Title

PHOTOEMISSION FROM NOBLE METALS AND ADSORBATES USING SYNCHROTRON RADIATION

Author

Shirley, D.A.

Publication Date

1977-07-01

Submitted to Physica Scripta

LBL-6650 c.1
Preprint

PHOTOEMISSION FROM NOBLE METALS AND ADSORBATES USING SYNCHROTRON RADIATION

D. A. Shirley, J. Stöhr, P. S. Wehner,
R. S. Williams, and G. Apai

July 1977

Prepared for the U. S. Energy Research and
Development Administration under Contract W-7405-ENG-48

PHOTOEMISSION FROM NOBLE METALS AND ADSORBATES USING SYNCHROTRON RADIATION[1]

D. A. Shirley, J. Stöhr, P. S. Wehner,
R. S. Williams, and G. Apai[2]

Materials and Molecular Research Division
Lawrence Berkeley Laboratory
and
Department of Chemistry
University of California
Berkeley, California 94720 U.S.A.

---

[1] This work was done with support from the U. S. Energy Research and Development Administration.

[2] Present address: Eastman Kodak Company, Rochester, New York 14650.

TABLE OF CONTENTS

Abstract

Photoemission from noble metals and adsorbates using synchrotron radiation. D. A. Shirley, J. Stöhr, P. S. Wehner, R. S. Williams, and G. Apai (Materials and Molecular Research Division, Lawrence Berkeley Laboratory and Department of Chemistry, University of California, Berkeley, California 94720 U.S.A.).
Physica Scripta (Sweden).

With the advent of synchrotron radiation in the 32-280 eV range at the Stanford Synchrotron Radiation Project, it has become possible to elucidate the transition from ultraviolet to x-ray induced photoemission. This has been accomplished by studies of noble metals. Polycrystalline copper shows a valence-band (VB) profile that approaches the x-ray induced shape at $h\nu \sim 100$ eV. In polycrystalline silver, the 4d cross-section follows the atomic curve, with a reversal of VB peak intensities near $h\nu = 110$ eV. Strongly anisotropic behavior is observed in copper single crystals, using angle-resolved photoemission (ARP). Normal ARP spectra from Cu(100), (110), and (111) crystals follow the band dispersion through the Brillouin Zone, including a dramatic resonance between the Fermi level (E_F) and 2 eV binding energy for $h\nu = 43$-52 eV. High temperature and high photon energy studies demonstrate the importance of the Debye-Waller factor in photoemission leading to a breakdown of the direct transition model. In adsorption studies of CO on Ni and Pt, CO is shown to stand up with oxygen out. For Pt, electrons are found to flow from t_{2g} orbitals near E_F to CO, and the CO 1π and 5σ binding energies are reversed relative to the gas phase. At higher photon energies, $h\nu = 150$ eV, the CO orbitals are very prominent on a Pt substrate. An inversion of the angular distribution of these orbitals and energy-dependent resonances in their intensities provide evidence for final state scattering effects at photon energies above 40 eV.

1. Introduction

Historically, the available laboratory photon sources caused an artificial division of photoelectron spectroscopy into an ultraviolet (UPS) regime and an x-ray (XPS) regime. While UPS ($h\nu < 41$ eV) employed gas discharge lamps, XPS ($h\nu > 1254$ eV) made use of characteristic x-ray lines. The spectral range between these energies remained essentially untouched until the high-intensity continuum of synchrotron radiation was utilized. [1] In this paper we report photoemission studies carried out in the transition region between UPS and XPS energies using synchrotron radiation emitted by the storage ring SPEAR at the Stanford Linear Accelerator Center. [2] It is our purpose to present a unified description of a series of investigations that bridge the UPS-XPS gap. To this end we present a considerable amount of new data and also summarize briefly other work published elsewhere. Besides facilitating experiments in a previously inexcessible energy range, synchrotron radiation offers other advantages; i.e., continuous tunability and a high degree of polarization. [1] We have utilized these features to study photoemission from valence levels of Group IB metals (Cu, Ag, and Au) and adsorbates on catalytic substrates (i.e., CO on Ni and Pt).

A goal of this work is to elucidate the transition in valence band (VB) photoemission spectra of noble metals from sharply structured direct-transition features at UPS energies to density-of-states like spectra at XPS energies. We also discuss various types of photon-energy-, polarization- and emission-angle-dependent cross section effects for d-band metals and adsorbate systems. Section 2 deals with the resolution, intensity, and spectral range of monochromatic radiation used in the present experiments. Section 3 presents results on atomic cross-section effects in Cu(3d), Ag(4d), and Au(5d) valence bands and their role in the evolution from UPS to XPS spectral behavior. Section 4 discusses band structure effects observed in both angle-integrated and angle-resolved photoemission from copper. These results demonstrate for the first time that energy-dependent normal emission from low-index single crystal faces in the newly available energy range $h\nu$ = 32-280 eV maps out the band structure along symmetry lines throughout the entire Brillouin Zone (BZ). They also show the importance of photoelectron refraction at the surface in non-normal emission. The influence of the Debye-Waller factor on valence-band photoemission spectra is discussed in Section 5, and we show that indirect transitions become important at high temperatures and high photon energies. Section 6 reports angle- and energy-dependent studies of CO adsorbed on Ni(111) and Pt(111) surfaces. Angle-integrated photoemission is shown to yield the relative intensities of adsorbate and substrate valence levels as a function of photon energy. Angle-resolved photoemission provides further information on molecular bonding and orientation. Finally we present experimental data which appear to indicate final state scattering effects in angle-resolved photoemission from CO on Pt(111). Section 7 summarizes the conclusions drawn from this work.

2. The Photon Source

A number of electron storage rings that can provide synchrotron radiation for photoemission studies are now available or under construction throughout the world. [1] Among these, a smaller group of intermediate- and high-energy machines afford the possibility of bridging the entire gap between ultraviolet and x-ray energies available from laboratory sources. The Stanford Synchrotron Radiation Project (SSRP) [2] has the capability of doing ultra-high vacuum photoemission studies up to and somewhat beyond the carbon K-edge energy of 280 eV. No facility has the capability at present to do photoemission at higher energies; i.e., all the way up to x-ray energies. The work reported here was carried out in the 32-250 eV range using the 4° port on Beam Line I at SSRP.

The grazing incidence monochromator ("grasshopper") installed on the 4° port [3] is equipped with a 600 ℓ/mm grating, yielding high intensity radiation with sufficient resolution (<1 eV) for photoemission studies between 32 and about 280 eV. Above 280 eV the intensity decreases dramatically due to ubiquitous carbon contamination on the reflecting surfaces. Figure 1b shows the transmission of the grasshopper monochromator measured as the photocurrent of an Al_2O_3 photodiode [4] (Fig. 1a) as a function of photon energy. To obtain the absolute flux out of the monochromator, the curve shown in Fig. 1b must be corrected by the photoyield of Al_2O_3 which, unfortunately, is known only for $h\nu \leqslant 160$ eV. [5] Figure 2 shows the quantum efficiency of our detector in the range $10 \text{ eV} \leqslant h\nu \leqslant 160$ eV. [5] Since the quantum efficiency varies by less than ±20% between 40 and 160 eV, Fig. 1b should describe the energy variation of the photon flux fairly accurately. Table I lists the photon flux (photons $sec^{-1}mA^{-1}mrad^{-1}$) emerging from the monochromator in the energy range 32-290 eV [6], calculated from the cathode current of the photodiode utilizing the Al_2O_3 quantum efficiency values (also in Table I).

In order to compare the photon flux emitted by the storage ring SPEAR to that emerging from the monochromator, the resolution of the monochromator must be considered. The monochromator bandwidth ΔE (in eV) is theoretically given by the relation [7]

$$\Delta E = 8 \times 10^{-6} \quad E^2 \quad , \tag{1}$$

where E is the photon energy in eV. Values for ΔE in the range 32-290 eV are listed in Table I. Integrating the respective $\Delta E/E$ values to yield a 10% bandwidth ($\Delta E/E = 0.1$) we obtain the photon flux values listed in the last column of Table I. These values can now be directly compared to the flux emitted by SPEAR as shown in Fig. 3. During the course of our experiments SPEAR operated at 3.3 GeV producing a photon flux of 2-5 × 10^{12} photons $sec^{-1}mrad^{-1}mA^{-1}$ $(10\% \text{ bandwidth})^{-1}$ (see Fig. 3) in the energy range 30-300 eV. Thus, for maximum monochromator transmission ($h\nu = 150$ eV) the efficiency of the optical system (consisting of 4 mirror reflections and the diffraction grating) is about 0.15%. This is actually an upper limit since contributions from higher order harmonics and scattered light to the transmitted radiation have been ignored. Also we have assumed that the bandwidth of the monochromator is given by Eq. (1), which is the optimum value achievable.

3. Atomic Cross-Section Effects in Noble Metals

3.1 Total d-band Intensity

Cooper and Fano [8] predicted minima in the atomic photoemission cross-section if the initial state wavefunction exhibits a radial node. In such cases the cross-section may vary strongly over a small energy range. We have investigated whether such effects can be observed in photoemission from VB in solids. We have studied the energy dependence of the d-band intensity in Cu (3d, no radial node), Ag (4d, one radial node), and Au (5d, two radial nodes) in the range $40 \text{ eV} \leqslant h\nu \leqslant 250 \text{ eV}$.

Results for Cu, Ag [9] and Au [10] are shown in Fig. 4. The energy dependence of the d-band intensity is significantly different for the three metals. The d-band intensity varies the least for Cu, with a maximum around 130 eV. For Ag a strong intensity variation is observed with a maximum around 60 eV and a minimum at 140 eV. The intensity changes most dramatically, by a factor of $\sim$10, between 100 eV and 130 eV. The Au valence band also exhibits its maximum intensity at low photon energy ($\lesssim$40 eV) with a pronounced decrease, by a factor of 30, between 70 eV and 160 eV. Unfortunately, our measurements for Au extend only to 190 eV, because the low photon flux (see Fig. 1) combined with the small d-band cross-section did not allow us to obtain spectra at higher energy.

As discussed in Ref. 9 the measured d-band intensities should be approximately proportional to the photoionization cross-sections for the 3d, 4d, and 5d levels in atomic Cu, Ag, and Au, respectively. The selection rules for electric dipole transitions ($\Delta \ell = \pm 1$) connect a d initial state to p- and f-partial-wave final states. The important variations in Fig. 4 can be discussed in terms of the d → f channel, which is dominant (relative to d → p) at high energies (>20 eV). [8] Above threshold the d-band intensities first exhibit maxima which occur in the order Au 5d (<40 eV), Ag 4d (≈60 eV), and Cu 3d (≈130 eV). Such maxima have also been observed in absorption measurements above the d-threshold. [11] The reason for this shift in maximum cross-section is that, close to threshold, the f radial final state function is restrained to be far from the nucleus by the centrifugal barrier $\ell(\ell+1)/r^2$; thus little overlap is possible with the initial state d-function. As the kinetic energy increases the εf wavefunction begins to have greater overlap with the d-function, creating a larger cross-section. Because the orbital radial expectation values decrease in the order 5d > 4d > 3d, maximum overlap, and hence a maximum in cross-section beyond threshold, will occur in the same order, as observed. At higher energies the d-band intensity decreases steeply to a minimum for Ag and Au. These so-called Cooper minima arise from a change of sign in the radial dipole matrix element associated with the d → f channel. The photoexcitation cross section, which is proportional to the sum of the squares of the p and f channel radial matrix elements, will exhibit a minimum at the energy for which one of the matrix elements vanishes. In general, a minimum in the cross-section can occur provided the initial state wavefunction has at least one node. As compared to the 4d function in Ag (one node) the 5d function in Au has two radial nodes and the 5d → εf matrix element approaches zero more gradually. In this case the Cooper minimum is smeared out.

3.2 Effect on the d-band Fine Structure

The atomic cross section effects discussed above can also influence the detailed shape of the valence band spectra and hence play an important role in the transition from UPS to XPS-like VB spectra. Because atomic cross section effects are most pronounced for 4d initial states, we shall discuss Ag as an example. [9]

Figure 5 shows high resolution spectra obtained from the VB of Ag in the energy range 60 eV $\leqslant h\nu \leqslant$ 150 eV. Characteristic features are the flat s-band extending beyond 3 eV binding energy (E_B) below the Fermi level (E_F) and the two prominent d-band peaks centered at ∿4.8 eV and ∿6.3 eV E_B, respectively. The d-band peak positions remain unshifted with photon energy and only the relative peak heights change. The most noticeable changes occur in the photon energy range 110-130 eV, where the relative heights of the two leading d-peaks are inverted in comparison to that observed at the other photon energies. Finally, at the lowest and highest photon energies the d-band structure resembles the XPS (Al Kα 1486.6 eV) spectrum shown at the top of the figure.

Comparison of Figs. 4 and 5 reveals a close correspondence between the slope of the curve in Fig. 4 and the intensity ratio of the two prominent valence band peaks in Fig. 5. In the range of steepest slope, i.e., for 100 eV $\leqslant h\nu \leqslant$ 130 eV, changes of approximately 20% in cross section occur over an energy interval of $\Delta E \sim 2$ eV, which is approximately the separation of the two prominent VB peaks (Fig. 5). Figure 6 shows schematically, for ∿120 eV photon excitation, the consequences of this variation. The higher E_B peak is predicted to have a larger cross section than the lower E_B peak and thus increase in relative intensity, in agreement with experiment. Thus, for the case of polycrystalline silver, we conclude that the transition from an UPS-like to an XPS-like VB spectrum is not achieved before photon energies of at least 150 eV. Similar behavior is expected for other 4d-group (and for 5d-group [12]) elements.

4. Band Structure Effects in Copper

4.1 Polycrystalline Cu

The noble metals have been the subject of numerous investigations using both ultraviolet [13] and x-ray photoemission. [14] The UPS spectra display structure characteristic of the energy distribution of the joint (initial and final) densities of states, [13] whereas XPS measurements are generally acknowledged to reflect the initial densities of states. [14] We have recently investigated the transition from UPS to XPS spectra by studies of the valence bands of polycrystalline Cu in the photon energy range 40 eV $\leqslant h\nu \leqslant$ 200 eV. We present first our angle-integrated photoemission (AIP) results on polycrystalline copper. [15]

Typical results obtained from the valence bands of polycrystalline Cu are shown in Fig. 7. All spectra have in common the three peaks at $\sim$2.5 eV, $\sim$3.6 eV, and $\sim$4.7 eV E_B relative to the E_F. The most distinct changes in the shape of the VB spectra occur between 50 and 70 eV; while the peak positions in this range remain virtually unchanged, the relative intensity of the peak at $\sim$3.6 eV E_B increases with photon energy. This trend continues above 70 eV in a less spectacular way, resulting in a slightly broader overall structure which, at photon energies above 90 eV, strongly resembles the spectrum observed with Al Kα radiation, shown at the top of Fig. 7.

This rapid transition from the UPS regime to the XPS limit arises from several factors: 1) an increase in the number of allowed direct transitions due to the increase in the number of final states available; 2) a more complete sampling of the first BZ arising from an uncertainty in the final state momentum, and 3) an increase in the number of indirect (i.e., phonon-assisted) transitions at the higher photon energies. The last effect, however, under the experimental conditions employed here, has been demonstrated by angle-resolved work performed on single crystals to be negligible. This will be discussed below.

To determine the relative importance of the first two effects, theoretical spectra were calculated using two different models. In the first set of calculations a direct transition (i.e., $\vec{k}$-conserving) model of photoemission was tested. In this approximation, the photoelectron energy distribution PED is given by [13]

$$N(E, h\nu) \propto \int_{BZ} d^3k_i \sum_{i,f} |\langle \phi^f(\vec{r})|\vec{A}\cdot\vec{p}|\phi^i(\vec{r})\rangle|^2 \, \delta(\vec{k}_f - \vec{k}_i - \vec{k}_{h\nu} - \vec{G}) \times$$

$$\times \; \delta(E_f(\vec{k}_f) - E_i(\vec{k}_i) - h\nu) \; \delta(E - E_i(\vec{k}_i)) \quad . \qquad (2)$$

Here $\phi^f(\vec{r})$ and $\phi^i(\vec{r})$ are the electron wavefunctions of an initial state of wavevector $\vec{k}_i$ and energy E_i and a final state of wavevector $\vec{k}_f$ and energy E_f, respectively. The δ-functions represent the requirements of momentum (wavevector) and energy conservation in the excitation process, with that for momentum resulting from a sum over lattice sites. $\vec{k}_{h\nu}$ is the photon wavevector and $\vec{G}$ is a reciprocal lattice vector. Spectra measured for various detector positions are identical (apart from possible changes caused by surface effects at low take-off angles).

In this case one can envision the photoeffect in the following way. Any transition that conserves energy and momentum produces a photoelectron which can be detected. The PED is thus determined by all possible excitations (sum over the BZ).

In order to evaluate Eq. (2) detailed knowledge of both the initial and final state band structures is required. Unfortunately, the description of the final state band structure is difficult for excitation energies greater than 40 eV; very few band structure calculations have been made at such high energies. Therefore, we have assumed that the free electron dispersion relationship [16]

$$E_f(\vec{k}) = (\hbar^2/2m)|\vec{k} + \vec{G}|^2 \quad , \tag{3}$$

where $\vec{k}$ is the crystal momentum in the reduced zone scheme, adequately describes the final-state band structure. The zero of the free electron bands was taken to coincide with the bottom of the 4s-like band in the initial-state Cu band structure, $E_i(\vec{k})$. Smith's [17] parameterization of the LCAO interpolation scheme of Hodges, Ehrenreich, and Lang [18] was used to generate $E_i(\vec{k})$. Effects due to matrix elements, as contained in the term

$$|\langle \phi^f(\vec{r})|\vec{A}\cdot\vec{p}|\phi^i(\vec{r})\rangle|^2 \tag{4}$$

were neglected except in relation to the relative cross section of 4s and 3d wavefunctions. In each case when an allowed transition was found, it was weighted by the <u>sum of the squares</u> of the coefficients multiplying the five atomic d-functions in the normalized LCAO wavefunction $\phi^i(\vec{r})$. The s contribution to the initial-state wavefunction was given zero weight to account, at least partially, for the large difference between s- and d-photoemission cross sections. Details of the $\vec{k}$-integrations are given in Ref. 15. A similar calculation was made in Ref. 15, but it differed in that an attempt was made to evaluate angle-dependent matrix elements, as noted at the end of this subsection.

The second calculation differed only in that the requirement of strict $\vec{k}$-conservation for a transition was relaxed to account for uncertainty in the final-state momentum. As discussed in detail by Feibelman and Eastman, [19] and recently by Feuerbacher and Willis, [20] an uncertainty or smearing in the final state momentum normal to the surface results when the source region of the photocurrent is restricted near the surface, as is the case in the present study [21,22] (see Fig. 8). To incorporate this uncertainty in the final-state momentum ($\vec{\Delta}$) in our calculations, all final states with wavevectors $\vec{p}$ and energy $E_f(\vec{k}) = (\hbar^2/2m)|\vec{p}|^2$ which satisfied $(\vec{k} + \vec{G}) - \frac{1}{2}\vec{\Delta} \leqslant \vec{p} \leqslant (\vec{k} + \vec{G}) + \frac{1}{2}\vec{\Delta}$ for a given free electron final state $\vec{k} + \vec{G}$ in Eq. (3), were allowed. To estimate the magnitude of $\vec{\Delta}$, the uncertainty principle ($\Delta k \Delta x = \frac{1}{2}$) was invoked, and values for Δx were those determined for the mean free path of an electron in copper as a function of final-state energy (see Fig. 8). The maximum amount of smearing (broadening) calculated in this fashion corresponds to only ca. 10% of the width of the first BZ, and can be as small as 3% for the lowest-energy photoelectron spectra reported here.

Results of the calculation assuming direct transitions (model I), convoluted with a 0.5 eV FWHM Gaussian, are shown in Fig. 9a. Comparison of these calculated PED's with the experimental curves in Fig. 9b reveals that fair agreement exists at $h\nu = 50$ eV. For photon energies greater than 50 eV, however, the calculated PED's compare very poorly with experiment. For example, at $h\nu = 60$, 90, 150, and 200 eV, four peaks are predicted, whereas only three are observed. Other points of disagreement are found in the detailed shape of the spectrum; for example, the higher E_B peaks at $h\nu = 60$ and 70 eV are predicted to be too intense, while at $h\nu = 175$ eV they are predicted to be too weak. The most serious discrepancy between theory and experiment, however, is the failure of the calculated curves to converge to a limit as the photon energy is increased.

In Fig. 9c we present the results of the calculations (convoluted with a 0.5 eV FWHM Gaussian function) in which final-state momentum broadening was included (model II). The amount of broadening $|\vec{\Delta}|$ at each energy is given in the figure. The calculations predict essentially constant peak positions, at $\sim$2.5 eV, $\sim$3.5 eV, and $\sim$4.6 eV E_B over the entire photon energy range, in complete agreement with experiment. When compared to the experimental results in Fig. 9b good agreement of trends in peak intensity with energy is also found to exist over the entire photon energy range; for example, the buildup of the peak at $\sim$3.5 eV E_B as the photon energy increases from 50 to 70 eV is correctly predicted. Similarly, above 90 eV the spectra are predicted to be uniform in shape and are virtually identical to the density of states (compare top of Fig. 9c), in agreement with experiment. Indeed, the calculated PED's are found to correspond very well with the experimental spectra except for the slightly exaggerated peak structure. This difference, however, arises mainly from the initial-state band structure, as illustrated at the top of Fig. 9, where the Cu 3d density of states (column (c)) is compared to the experimental PED measured with Al Kα radiation (column (b)). In particular, the peak structure is generally too pronounced and the middle peak is too high. Thus for polycrystalline Cu, uncertainty in the final state momentum is crucial in determining the photon energy at which the XPS limit is reached, consistent with previous predictions. [19]

The conclusion drawn above is the same conclusion given in Ref. 15: viz, that momentum broadening is needed to fit the polycrystalline Cu d-band photoemission spectra in the direct transition model. However, the details of the two calculations are quite different, and the differences are important. In Ref. 15, we included "matrix-element" integrals (Eq. (4)) in the orthogonalized plane-wave final state approximation in the expectation that this would be better than ignoring matrix-element effects altogether. However, the description of the final state wavefunction is still a major problem in the calculation of photoemission spectra. It appears from the calculations of Janak, et al. [23] and Wagner, et al. [24] that for copper comparable or better fits to the spectra are obtained if matrix element effects are completely omitted. Furthermore, it is difficult to include momentum broadening in the evaluation of the transition matrix element. We therefore feel that the present approach of assuming constant matrix elements is more appropriate than that of Ref. 15.

4.2 Angle-Resolved Photoemission From Cu(001), (110), and (111) Single Crystals

In contrast to the results for polycrystalline Cu presented above, angle-resolved spectra obtained from the three low-index crystal faces of Cu; i.e., the (001), (110), and the (111) faces, are found to be very rich in structure. [10,25] This is illustrated in Fig. 10, where we show representative spectra acquired from the three low-index faces in normal emission for 32 eV $\leqslant h\nu \leqslant$ 160 eV. Considerable variations in both peak intensities and positions occur throughout the energy range studied. In Part 4.21 of this section, we will demonstrate how variation in peak positions can be related directly to the bulk band structure using a direct transition model of photoemission. In Part 4.22 we treat the problem of non-normal emission with particular emphasis on the matching conditions at the surface.

4.21 Normal Emission

The interpretation of ARP spectra in terms of electronic band structure has suffered from a lack of detailed information on how the crystal momentum $\vec{q}$ of the photoexcited electron inside the crystal is related to the momentum $\vec{p}$ of the free electron outside the crystal. Normal photoemission avoids this problem because electron refraction at the surface is zero and the propagation direction of the electron inside and outside the crystal is the same. Thus the detailed relationship between $\vec{q}$ and $\vec{p}$ need not be considered.

Typical results obtained from the three low-index faces of Cu in normal emission for 32 eV $\leqslant h\nu \leqslant$ 160 eV are shown in Fig. 10. Several important features to note in these spectra are: 1) the distinct differences in spectra taken at the same photon energy but along different directions; 2) the absence of an s-p band ($E_F \leqslant E_B \leqslant 2$ eV) at certain photon energies, e.g., between hν = 70 eV and hν = 100 eV in the [110] direction; 3) the strong "s-p resonance" at $E_B \sim 0.5$ eV in the [110] direction at hν = 45 eV, and 4) the variation in the d-band spectral width (2 eV $\leqslant E_B \leqslant$ 6 eV) as a function of photon energy, e.g., varying from ∿1.3 eV wide at hν = 32 eV to ∿3.5 eV wide at hν = 100 eV in the [001] spectrum.

Comparison of the spectra in Fig. 10 to those obtained from polycrystalline Cu (Fig. 7) shows that the angle-resolved spectra exhibit substantially different structure and evolution of features than do the polycrystalline results. The increased richness in the angle-resolved spectra can be traced to two sources: 1) the orientation of the electric field vector ($\vec{E}$) of the light relative to the crystalline axes, and 2) the position of the detector relative to the crystalline axes.

For angle integrated photoemission from polycrystalline samples the effects of incident light polarization relative to crystalline axes are averaged out because all crystalline orientations relative to the electric field vector occur with equal probability. On the other hand, for ARP from single crystals there is a unique orientation of the $\vec{E}$ vector with respect to the crystalline axes; thus, ARP spectra are sensitive to both the photoelectron momentum and the radiation polarization, with respect to the crystalline axes. Having noted the importance of polarization effects in ARP, we refer to the work of others on this subject. [26] The main thrust of our work has been the elucidation of point 2 above.

The spectra measured in ARP depend on the detector position relative to the crystalline axes. This follows because among the allowed transitions only those are sampled for which the photoelectron momentum vector points into the detector. As a result, only a small fraction of the initial and final states in the BZ contribute to the spectrum. For example, consider emission in the [001] direction from a single crystal, as shown schematically in Fig. 11b. Here we have assumed an angular resolution of ±5° and the direct transition model discussed above. The constraints of conservation of momentum and the directionality of the photoelectron momentum vector ($\vec{q}$ must point toward the detector) severely limits the amount of the first BZ (to a section of a spherical surface) which can contribute to the photoemission spectrum. If uncertainty in the final state momentum is included a slightly larger portion of the BZ can contribute (see Fig. 11c). Thus, variations in the ARP spectrum with angle or energy arise in this model because different parts of the first BZ are being sampled.

Calculations using Eq. (1), where the sum over $\vec{k}_f$ has been restricted to just those $\vec{k}_f$-values which can be observed but neglecting matrix elements and the uncertainty in $|\vec{k}_f|$, have been performed by Wagner, et al. [24] for emission in the [001] and [111] directions and by our group [25] for emission in the [110] direction. In both sets of calculations there is excellent agreement with all major changes in structure occuring as functions of photon energy. The positions and overall widths of most of the peaks were also reproduced well in the calculations. An example of the type of agreement obtained is shown in Fig. 12 where we present the results of a calculation for photoemission in the [110] direction at a photon energy of 45 eV. As seen in the figure, the overall concurrence in peak positions and widths is very good; note, in particular, that the pronounced "s-p resonance" observed experimentally is predicted in the calculations.

Perhaps a more instructive way of viewing the results is shown in Fig. 13. Here the experimental peak positions $E_{ex}(\vec{k})$ are compared with Burdick's [27] band structure of Cu. The locations of the experimental points in the figure were derived as follows. From the measured peak positions, relative to the E_F, the final state energy $E_f = E_{ex}(\vec{k}) + h\nu$ was calculated. The magnitude of the final state wave vector was then determined from the free electron dispersion relationship $|\vec{q}| = (2mE_f/\hbar^2)^{1/2}$, where the zero of the free electron scale was taken to be the bottom of the free-electron-like bands in Burdick's band structure. The relations $\vec{k}_{\parallel} = 0$ and $\vec{q}_{\perp} = \vec{k}_{\perp} + \vec{G}_{\perp}$, where $\vec{G}$ is a reciprocal lattice vector, then yield $\vec{k}$ in the first BZ and the corresponding values $E_{ex}(\vec{k})$ are plotted as bars in the figure. The inset at the bottom of each panel establishes a correspondence between photon energy and the part of the BZ sampled.

Comparison of our experimental peak positions with Burdick's band structure in Fig. 13 reveals generally good agreement. In particular, the pronounced "s-p resonance" for photoemission in the [110] direction at $h\nu = 45$ eV is fully explained in terms of bulk transitions arising from a well-defined part of the BZ (points near $\vec{k} = (-0.5, -0.5, 0)$). The appearance of an s-p band at only certain photon energies is explained as well. Only when photoemission occurs in a part of the zone where a band exists near the E_F is an s-p band observed, e.g., for photoemission in the [111] direction at hν = 70 eV, states near L are sampled (see Figs. 10c and 13c). Finally, the variation in the width of the d-band is also easily understood in terms of the dispersion of the bands across the zone.

To illustrate further the direct relation between photoemission spectra and band structure for copper in this energy range, it is instructive to compare Fig. 10a with Fig. 13a. Both pertain to the [001] direction. Varying the photon energy from 32 eV up to 160 eV yields first a narrow peak, evolving into two widely-spaced peaks, then back to a relatively narrow peak again (Fig. 10). But this is exactly as expected in going from Γ in the second zone through X to Γ in the third zone (Fig. 13).

A closer examination of Figs. 10 and 13, however, reveals two interesting facts: 1) in all three directions studied, a band exists between $6\text{ eV} \leqslant E_B \leqslant 9\text{ eV}$ in the band structure but no peaks are observed at a E_B greater than 6 eV; and 2) for photon energies near 130 eV and emission in the [110] direction, the same portion of the BZ is sampled as at hν = 45 eV but, in contrast to the hν = 45 eV spectrum, no strong peak is observed in the s-p region of the spectrum. The first observation is readily explained by the relative cross section of 4s and 3d wavefunctions, as discussed in Part 4.1 (a tight binding calculations shows the composition of the states spanning the range $6\text{ eV} \leqslant E_B \leqslant 9\text{ eV}$ to be almost completely "s" in character). The second observation can be attributed to the increased volume sampled in the BZ because of the smaller inelastic mean free path in the 130-140 eV region ($\lambda_e \sim 3$ Å) as compared to that around 45 eV ($\lambda_e \sim 8$ Å) (Fig. 8), and the increased radius of the cylinder detected in k space (Fig. 11). While this broadening is small for electron energies near 45 eV (only ∿3% of 2π/a), it amounts to ∿10% of the width of the BZ in the range 130-140 eV. This amount of broadening is sufficient to smear out the sharp peak (an intense shoulder is observed) in the s-p band because of the steepness of the band from which this structure arises (see Fig. 13b). Indeed, momentum broadening in the final state poses a serious problem in the use of photon-energy-dependent ARP studies (as employed here) to map out the details of the bulk band structure.

We close this subsection by noting that the effective photon energy in which dispersion relations can be determined is rather narrow. At the lowest energies (∿10 eV) band-structure effects distort the free-electron nature of the final states. There is a usable region (roughly 20-80 eV) in which the electron mean free paths are still relatively long (see Fig. 8), permitting sharp features to be observed. At higher energies (∿100 eV) the broad minimum in the electron-mean-free-path relation is approached, and $\vec{k}$-broadening obviates sharp structure in the spectrum. Fortunately the intermediate region is usually wide enough to permit studying the entire first BZ.

4.22 Non-normal Emission

For non-normal emission the relation between $\vec{q}$ and $\vec{p}$ must be considered explicitly, because the propagation directions of the electron inside and outside the crystal need not be the same due to the presence of a potential barrier at the surface. With a simple free-electron description of the final state and the assumption of specular boundary conditions, the following relationships between $\vec{q}$ and $\vec{p}$ follow [28]:

$$\vec{p}_{\parallel} = \vec{q}_{\parallel} \quad ,$$

$$|q_{\perp}|^2 = |p_{\perp}|^2 + 2mV_0 \quad , \qquad (5)$$

where m is the mass of the electron and V_0 is the inner potential.

To determine the accuracy of this expression for describing non-ideal systems, we have performed ARP experiments on (001), (110), and (111) Cu single crystals, in all cases at a photon energy of 45 eV and in a [110] emission direction (for (001) and (111) crystal faces, [110] directions fall at 45° and 35° away from the normal, respectively). These particular experiments were chosen due to the presence of an extremely sharp resonance in the s-p band of Cu at this energy (see Fig. 10), which is very sensitive to the exact portion of the BZ being sampled. This peak (the "band 6 peak") arises only through transitions from the 6^{th} valence band which goes steeply through E_F between Γ and K as shown in Fig. 13.

In Fig. 14 we present the results of this study. Here the relative area under the band 6 peak is plotted as a function of the emission angle (Θ), measured from the sample normal. Results obtained from (110) crystals, Figs. 14b and 14d, show that the maximum in intensity of the band 6 peak occurs for normal emission, i.e., along the [110] direction. The difference in the detailed shapes of the two curves arises from the fact that the $\vec{E}$ vector of the incident light does not lie in the same crystalline plane. Inspection of Figs. 14a and 14c show that this maximum in intensity is shifted from the bulk [110] crystalline direction for emission from (001) and (111) single crystals, indicating refraction of the photoemitted electrons at the crystal-vacuum interface. The resulting refraction angles are ∿15° and ∿12° for emission in the [110] direction from the (001) and the (111) crystal, respectively.

Comparison of these refraction angles to those determined using Eq. (5), which yields values of 10° and 7° for emission in the [110] direction from (001) and (111) single crystals, respectively, shows that fair agreement is obtained. There is, however, a discrepancy of 5°, the calculated values being smaller than those observed experimentally. This discrepancy is not yet understood and is under further study. A longer manuscript is under preparation [29] which will be devoted to refraction effects. However, we can already conclude that the preliminary results reported here establish for the first time that free-electron matching conditions at the surface provide an adequate first approximation to the relationship between the propagation direction of the electron inside the crystal and that outside the crystal.

5. Thermal Disorder and Indirect Transitions in Photoemission.

This section deals with the breakdown of the direct-transition model discussed above. Shevchik [30] pointed out that the photoemission cross-section from a solid must contain a Debye-Waller factor, and he predicted that this would favor indirect (i.e., phonon-assisted) photoelectron excitation at high temperatures or photon energies. We have observed this effect for the first time. [31] These results show that high-temperature or x-ray induced photoemission does not follow the direct transition model but rather samples much of the BZ.

The temperature and energy dependence of the momentum conservation rules for elastically scattered radiation (e.g., x-rays, neutrons or electrons) by a crystal lattice is governed by the Debye-Waller factor

$$f = \exp\left[-\langle(\vec{q}\cdot\Delta\vec{r})^2\rangle\right] \quad . \tag{6}$$

Here $\vec{q} = \vec{k}_f - \vec{k}_j$ is the difference between the wavevectors of the incident ($\vec{k}_j$) and scattered ($\vec{k}_f$) radiation and $\Delta\vec{r}$ is the instantaneous thermal displacement of an atom from the equilibrium lattice position. In a simple one-electron picture, photoemission can be viewed as a scattering process. The initial state involves a photon with wavevector $\vec{k}_{h\nu}$ and a bound (e.g., a valence) electron with wavevector $\vec{k}_i$ ($\vec{k}_j = \vec{k}_{h\nu} + \vec{k}_i$), while the final state is characterized by the photoelectron with wavevector $\vec{k}_f$. The diffraction law $\vec{k}_f - \vec{k}_j = \vec{G}$, where $\vec{G}$ is a reciprocal lattice vector describing the elastic scattering of radiation by a crystal lattice, also describes the direct transition requirement in photoemission (Eq. (2)). Hence, one would expect the intensity of direct-transition features in ARP spectra to exhibit a temperature and energy dependence in accordance with Eq. (6).

In this approximation, the indirect transition channel in photoemission corresponds closely to x-ray temperature-diffuse scattering. [32] The connection between x-ray diffraction and ARP is revealed by an evaluation of the photoexcitation matrix element from Eq. (2), including the time average over the atomic thermal displacements,

$$|\langle \phi^{f}(\vec{r})|\vec{A}\cdot\vec{p}|\phi^{i}(\vec{r})\rangle|^{2} \sim f\,\sigma_{if}(\vec{k}_{f}) \left\{ \delta(\vec{q}-\vec{G}) + \left(1-\delta(\vec{q}-\vec{G})\right) \left[\phi_{1}\frac{|\vec{q}|^{2}}{|\vec{q}-\vec{G}|^{2}}(k_{B}T) + \phi_{2}|\vec{q}|^{4}(k_{B}T)^{2} + \dots \right] \right\} . \tag{7}$$

This expression was derived assuming an LCAO tight-binding initial-state and plane-wave final-state wavefunctions. Here, $\sigma_{if}(\vec{k}_f)$ is an atomic-type matrix element, k_B the Boltzmann constant, and T the temperature. The quantities ϕ_1 and ϕ_2 involve sums over phonon modes familiar from first- and second-order temperature-diffuse scattering. [32] It is assumed in this expression that the temperature is high enough for equipartition to hold for the phonon modes.

The importance of the direct ($\vec{q} = \vec{G}$) relative to the indirect transition terms in Eq. (7) depends on both *temperature* and *photon energy*. Although the photon energy does not explicitly occur in Eq. (7) it is contained in $|\vec{q}|$, since with increasing photon energy the photoelectron wavevector $\vec{k}_f$ (and hence $\vec{q} = \vec{k}_f - \vec{k}_j$) increases. The decrease of the Debye-Waller factor (Eq. (6)) is predicted to occur in discrete steps as a function of energy. As the photoelectron final-state crosses a zone boundary (with increasing energy), a new (longer) $\vec{G}$-vector enters the momentum conservation conditions, causing a decrease in the intensity of the direct-transition contribution to the photoemission spectrum.

To elucidate the effect of *temperature* on the ARP spectrum we again consider normal photoemission from a Cu(110) single crystal. At room temperature we found that photoemission from Cu in the ultraviolet (UPS) regime is dominated by direct transition processes (see Subsection 4.2 and Fig. 13). The band 6 peak at $E_B \sim 0.5$ eV for $h\nu$ = 45 eV is an extremely sensitive indicator of the direct transition channel because it can only originate from transitions in a very small region of the BZ. As phonon-assisted processes become more important with increasing temperature, this peak (Fig. 15) decreases dramatically in intensity, as expected. In Fig. 16a we have plotted the band 6 resonance intensity versus temperature. Also shown are plots of f^n ($n = 1,2,3$), where the values of $\langle \Delta r_x^2 \rangle$ used were bulk mean-square displacements for copper measured by x-ray temperature diffuse scattering. [33] The effective mean-square displacement seen in photoelectron spectra will be larger than the bulk value, however, due to the short electron mean-free path at this energy. For Cu the (110) interplanar spacing is 1.3 Å (half the nearest-neighbor distance), which indicates the photoelectron spectra of Fig. 15 are only sensitive to four (110) planes. Calculations for a (110) surface of Ni [34] have shown that mean-square displacements normal to the surface for a surface layer are as much as three times the bulk value, and decay exponentially to the bulk value by the fifth layer. Further calculations [35] indicate that the ratio of surface to bulk mean-square displacements increases with increasing temperature. Our data are consistent with these expectations; Fig. 16a shows the decrease in the band 6 resonance intensity corresponds to $2 > n > 1$ near room temperature and $n > 2$ at elevated temperatures.

Inspection of Fig. 15 shows that as the temperature is raised the shape of the d-band changes as well; the d-band peak becomes asymmetric, with more intensity at the top of the bands, until, at 800°C, the spectrum resembles that of polycrystalline copper for hν = 40-50 eV. [15] For copper, a single electron-phonon interaction can change the electron wavevector from the Γ point to anywhere within the BZ with no more than a 30 meV [36] change in the electron energy, thus allowing more of the $\vec{k}$ states in the BZ to be sampled without greatly disrupting their energy distribution. In Fig. 16b the ratio of indirect to direct transitions is plotted as a function of temperature, assuming two different values for the ratio at room temperature. This plot bears out the temperature dependence predicted by Eq. (7).

It follows that the direct-transition model describes ARP studies at ultraviolet energies only if the temperature is low enough to suppress phonon-assisted indirect transitions. Thermal mean-square displacements of atoms in crystals approach their limiting zero-temperature values for temperatures somewhat below the Debye temperature of the material in question. Thus, a general rule for assuming a minimum amount of thermal momentum broadening is to collect ARP spectra at temperatures below the surface Debye temperature.

Because the Debye-Waller factor determines the fraction of the $\vec{k}$-conserving direct transitions, the direct transition process is less important at x-ray energies than at UPS energies. In fact, since $|\vec{q}|$ is about 5 times larger at hν = 1486.6 eV (Al Kα radiation) than at hν = 45 eV, it is expected from Eq. (6) that room temperature XPS spectra are dominated by the phonon-assisted indirect transition process. Indeed, angle-resolved XPS spectra exhibit a considerably weaker angular dependence than UPS spectra. [37] Furthermore, valence-band spectra of Au single crystals yield identical results at hν = 1253.6 eV (Mg Kα) and 1486.6 eV for photoemission along the [001] and [111] directions. [38] These experimental findings lead to the conclusion that the entire BZ is being sampled at high (⩾1000 eV) photon energies. The angular dependence observed in XPS spectra arises from the photoexcitation matrix element $\sigma_{if}(\vec{k}_f)$ in Eq. (7). [39]

6. Angle- and Energy-Dependent Studies of CO on Ni and Pt

6.1. Cross Section Effects for CO on Ni, Pd, and Pt

In this section we report photoemission studies of CO on Pt(111) in the range 40-150 eV [40] and interpret earlier studies by Gustafsson, et al. [41] of CO on Ni and Pd. Our main goal is to discuss the value of photoemission experiments on an adsorbate-substrate system using variable photon energies not accessible with laboratory sources. Another purpose of this study was to learn how the photoemission spectrum of CO on d-band metals is modulated by cross-section effects as a continuation of the studies on clean d-band metals in Section 3, and to select the most appropriate energy range for angle-resolved studies on adsorbates, discussed below.

Experimental results for clean Pt(111) and Pt(111) + 5L CO are displayed in Fig. 17 as solid and dashed curves, respectively. (1L = 1 Langmuir = 1×10^{-6} torr sec exposure). Common features of all spectra are the two peaks at ∿8.7 eV and ∿11.8 eV E_B relative to the E_F, attributed to the $(5\sigma + 1\pi)$ and 4σ CO molecular orbitals, respectively. The CO spectral intensity relative to the Pt VB, while low for $\hbar\omega \leqslant$ 100 eV, increases steeply at higher energies and is about a factor of

4 stronger at 150 eV than around 80 eV. Figure 18 shows quanitatively how the intensity ratio of the (5σ + 1π) CO peak and the Pt 5d VB changes with photon energy.

We attribute this adsorbate relative intensity enhancement above 100 eV to the steep decrease of the Pt 5d intensity between 100 eV and 150 eV, as shown in Fig. 19. The energy dependence of the Pt VB intensity was measured in the same way as that of Cu, Ag, and Au discussed above, and the Au (cf. Fig. 4) and Pt 5d cross sections show a very similar dependence. In Fig. 19 we have also plotted the theoretical differential photoionization cross section of the (5σ + 1π) molecular orbitals of CO as a function of incident photon energy. Although we realize the limitations of a plane-wave (PW) final state calculation for CO for quantitative comparison with experimental cross-sections, we have used the PW CO cross-sections [42] shown in Fig. 19, for lack of any more reliable theoretical values, to predict the ratio of the integrated (5σ + 1π) CO peak intensity relative to the Pt 5d VB intensity. The results, shown inserted on a linear scale in Fig. 19, are in qualitative agreement with the experimental results in Fig. 18.

The above approach can also account qualitatively for the relative cross sections of CO on Ni and Pd. Gustafsson, et al. [41] found that the relative adsorbate signal falls off much more rapidly for CO on Ni than for CO on Pd. Ni is a 3d VB metal and should exhibit an increase in photoemission intensity to hν ≈ 120 eV, then a more gradual monotonic decrease in photoemission intensity with increasing photon energy, much like Cu (see Fig. 4). For this case the CO spectral intensity falls off more rapidly than the Ni VB intensity, particularly for hν < 120 eV, giving a steep monotonic decrease of the adsorbate signal relative to that of the substrate. On the other hand Pd is a 4d VB metal with a radial node in the 4d wavefunction and should exhibit a Cooper minimum similar to the 4d VB of Ag (see Fig. 4). We attribute the increase in relative adsorbate emission for Pd at hν > 80 eV to this Cooper minimum. The restriction of their photon energy to hν ⩽ 100 eV precludes Gustafsson, et al. from observing the full extent of MO enhancement. Fig. 20 compares the experimental data (hν ⩽ 100 eV) of Gustafsson, et. al for the ratios $\sigma_{CO}(1\pi + 5\sigma)/\sigma_{Ni}(3d)$ and $\sigma_{CO}(1\pi + 5\sigma)/\sigma_{Pd}(4d)$ with the ratios derived from PW theoretical CO cross-sections [42] and our experimental intensities for clean Cu and Ag (Fig. 4). The data have been normalized at hν = 40 eV. The agreement over the photon energy range 40-100 eV substantiates the qualitative arguments we have previously invoked. An extension of the calculated ratio for Ag and CO cross sections allow us to predict enhanced CO/Pd ratio results for photon energies up to 150 eV, as shown in Fig. 21. Our results indicate that studies of molecular orbitals of adsorbates such as CO on 4d or 5d VB substrates will benefit from synchrotron studies at high photon energies because of the enhancement of relative adsorbate spectral intensity.

6.2 Bonding of CO on Pt(111)

The adsorption of a molecule on a metal surface affects the bonding orbitals of both the adsorbate and substrate. Hence, by comparing photoemission spectra of the adsorbate-substrate system with those of the adsorbate and substrate alone, the bonding mechanism may be studied. We report below such a study of CO on Pt(111).

When CO chemisorbs on the (111) face of Pt, the valence band peak nearest the E_F always decreases in intensity relative to the other peaks in the Pt valence band. Figure 22 shows the decrease of this intensity in spectra at two different photon energies, for which the total spectral intensities of clean Pt and Pt + CO have been normalized with respect to photon flux. The effect is even more striking in the angle-resolved spectrum at 40.8 eV (HeII radiation) shown in Fig. 23a, which was recorded for electron emission 40° away from the sample normal (see Fig. 23b). This indicates that the states nearest the E_F donate electrons to the CO molecule as it chemisorbs. This observation is supported by work-function measurements.[43]

To determine the composition of the states nearest the E_F we have calculated the band structure of Pt using Smith's [44] parameterization of the Hodges, Ehrenreich, and Lang [18] tight binding interpolation scheme. Figure 24 shows the calculated total VB density of states and its decomposition into the t_{2g} and e_g components. The peak nearest the E_F is seen to arise mostly from t_{2g} orbitals. Because of the high surface sensitivity [21] of photoemission spectra at $h\nu = 70$ eV and $h\nu = 150$ eV, these spectral features arise largely from surface Pt atoms. Calculations by Desjonquères, et al. [45] show that modification of the bulk bands at the surface does not change the basic t_{2g} character of the valence band near E_F. The dramatic decrease in intensity of this peak on chemisorption of CO thus indicates the involvement of surface t_{2g} orbitals in the chemisorption bond(s).

The molecular orbital peaks of chemisorbed molecules in photoemission spectra shift differently depending upon whether or not they are involved in the chemical bonding to the surface. The binding energy of adsorbate valence orbitals is in general lowered relative to the gas-phase value by a relaxation energy originating from polarization of the substrate valence electrons to screen the adsorbate hole state. In addition to this final state effect bonding orbitals exhibit a shift to higher binding energy due to their polarization toward the substrate (initial-state effect).

Figure 25 shows angle-resolved spectra of CO on Pt(111) at HeII energy, recorded in the experimental geometry shown in Fig. 23b. With increasing angle Θ between the surface normal and the photoemission direction the the E_B ($\sim$9 eV) CO peak splits into a doublet leading to three CO peaks at 8.1 eV, 9.3 eV, and 11.7 eV E_B at $\Theta = 60°$. Calculation of the differential photoemission cross section [46] for a CO molecule standing up on the substrate (see section 6.3 below) favors 1π orbital intensity at high Θ values. We therefore assign the lowest E_B peak at 8.1 eV to the 1π molecular orbital. Thus, the ordering of the 1π and 5σ orbitals is reversed from that of CO gas [47] due to a shift of the 5σ bonding orbital to higher binding energy. This reversal was predicted in recent theoretical calculations by Batra and Bagus [48] and by Bagus and Hermann [49] and was observed experimentally by other groups for Ni(111) [50] and Pd(111) [51] substrates.

6.3 Orientation of CO on Ni(111) and Pt(111)

Davenport [46] presented scattered-wave (SW) Xα calculations of photoelectron angular distributions from the molecular orbitals of oriented CO molecules and pointed out that chemisorbed CO should display similar angular distributions provided that the molecular wavefunctions are not strongly perturbed by the substrate. In this section we discuss photoelectron angular distributions at $h\nu = 40.8$ eV from CO adsorbed on Pt(111) and Ni(111) surfaces in terms of Davenport's theoretical calculations. [52]

In Fig. 26c we have plotted the change of the peak $4\sigma/1\pi + 5\sigma)$ intensity ratio as a function of polar photoemission angle Θ defined in Fig. 26a, for CO chemisorbed on Ni(111) and Pt(111) surfaces. Comparison of this ratio for the adsorbate-substrate systems (Fig. 25c) with the scaled theoretical intensity ratio for an oriented CO molecule (Fig. 26d) strongly favors the configuration where CO stands up, with the C bonded to the substrate. Note in particular that the configuration with O bonded to the substrate can be excluded because the $4\sigma/(1\pi + 5\sigma)$ ratio vanishes for angles $\Theta \geqslant 20°$. The overall good agreement between the experimental curves in Fig. 26c and the solid curve in Fig. 26d is not expected to be perfect in detail, mainly because the 5σ orbital is expected to be perturbed through its interaction with the substrate [48] as discussed in the previous section.

6.4 Final-State Scattering Effects

Low energy electron diffraction (LEED) has been the technique of choice to characterize the crystallographic structure of clean and adsorbate-covered surfaces. [53] However, several factors have kept this technique in most cases from being more than a surface characterization tool. First, LEED studies of adsorbed molecules have been hampered by radiation damage and dissociation of adsorbates by the electron beam. [54] Electrons tend to be more damaging than photons because they have high probabilities per incident particle of exciting a valence electron, the beams have a greater flux, and the radiation is concentrated closer to the surface, with a high degree of collimation. [53] Secondly, LEED scattering requires ordered domains ∿500 Å in diameter because of limitations on the coherence width of the electron beam. Thus studies of low-coverage adsorbate overlayers and amorphous or disordered materials are difficult. The most severe problem, however, lies in the analysis of the scattered LEED intensities due to strong multiple-scattering effects.

Some of these problems are eliminated by studying photoelectron diffraction [55,56] rather than LEED. As illustrated in Fig. 27 for the case of CO on a substrate in a classicial picture, a photoelectron can makes its way to the detector either directly (channel 1) or by scattering from the atoms of the substrate (channel 2). Quantum-mechanically, the two channels correspond to the primary photoelectron-wave and the backscattered wave from the substrate. It has been predicted theoretically that interference of these waves can significantly alter the photoemission angular distributions. It is clear that photoelectron diffraction not only avoids the radiation damage problem of LEED but is also applicable to isolated adsorbate units or materials lacking long-range order. Furthermore, by using synchrotrom radiation the photoelectron kinetic energy may be tuned to maximize either channel 1 or 2. This way photoemission from valence orbitals of adsorbates may yield the bonding coordination via channel 1 and the site geometry via channel 2. Photoemission from adsorbate core levels provides an additional check of the site geometry via channel 2 and, in the case of an adsorbed molecule, may also determine the molecular orientation via channel 1 through polarization selection rules. [57] As yet, photoelectron diffraction has not been applied experimentally to this purpose, but in the following we present some data for CO on Pt(111) which appear to indicate for the first time the importance of final-state interference effects.

Several angle-resolved photoemission spectra for Pt(111) + 4L CO are shown in Fig. 28. Common features of all spectra are the two peaks at ∿9.2 eV (A) and ∿11.8 eV (B) which are assigned to the $(1\pi + 5\sigma)$ and 4σ CO molecular orbitals, respectively. Peaks A and B show strong variations with Θ, the angle between the crystal normal and the photoelectron propagation direction. The polarized nature of synchrotron radiation leads to an enhancement of the angular dependence at $h\nu$ = 40 eV. This is clearly shown in Fig. 29, which also gives details of the crystalline orientation with respect to the photon beam and the detector (Fig. 29b,c). Figure 29 shows that the molecular orbitals of CO are not only more intense with respect to the VB at 150 eV than at 40 eV but also that there is a dramatic reversal in the angular variation of relative MO peak intensities.

Figure 30 shows the relative peak intensities and the ratio $4\sigma/(1\pi + 5\sigma)$ for normal photoemission and for a 45° electron take-off angle over the entire 40-150 eV range. For normal emission, the 4σ

and the 1π + 5σ peak intensities show modulations in the range 40-150 eV, while the energy dependence is relatively smooth for a 45° electron take-off angle.

The observed modulations indicate the importance of final state interference effects, which have theoretically been shown to vary strongly with both energy and photoemission angle. [56] For a molecule on a substrate, however, final-state interference effects exist not only between channels 1 and 2, but channel 1 itself contains interference effects resulting from intramolecular scattering within the molecule. Intramolecular final-state interference effects are included in SW $X\alpha$ calculations and have been found theoretically [46] and experimentally [58] to lead to cross-section resonances at energies not too far (∿10-20 eV) above threshold. Without a detailed SW $X\alpha$ calculation for an oriented (gas phase) molecule at higher (>40 eV) energies, the origin of the resonances in Fig. 30 and the reversal in angular photoemission distributions in Fig. 29 therefore cannot be interpreted quantitatively. Analysis of the observed intensities should yield information about the conformation of CO on Pt(111) and improve our general understanding of final-state scattering effects.

7. Conclusions

This paper summarizes a program that has been designed to characterize photoemission in a new energy range, particularly between 32 eV and ∿200 eV. The following major original conclusions about photoemission in this energy range have been derived from this program.

1. Atomic cross-section effects can modulate photoemission intensities of d-band metals and alter the valence-band spectra.

2. Photoemission spectra of polycrystalline copper can be understood in terms of the direct-transition model if $\vec{k}$-broadening is taken into account, and the x-ray photoemission limit is reached at $h\nu \sim 100$ eV.

3. Angle-resolved normal photoemission from copper makes it possible for the first time to determine the band dispersion relations throughout the entire Brillouin Zone.

4. Electron refraction effects have been observed directly for the first time, using the band 6 resonance in copper.

5. Thermal disorder effects in photoemission have been observed and studied quantitatively. Zero-phonon photoemission corresponds to $\vec{k}$-conserving transitions, while phonon-assisted transitions do not conserve $\vec{k}$, but instead sample more of the Brillouin Zone. Thus temperature is an important parameter in photoemission.

6. At intermediate photon energies ($h\nu \sim 150$ eV) adsorbate molecular orbital peaks may be intense relative to substrate peaks.

7. Shifts and changes of intensity of adsorbate and substrate peaks are related to details of chemical bonding.

8. Carbon monoxide stands up, with oxygen out, when adsorbed on Pt(111) and Ni(111).

9. At energies of 150 eV, where the photoelectron de Broglie wavelength is comparable to interatomic distances, photoelectron diffraction effects have been observed for CO on Pt(111).

Table I. Photon Flux and Energy Resolution for SSRP 4° Line Monochromator

Photon energy (eV)	Quantum efficiency of detector	photons[c] / sec·mA·mrad (10^7)	Monochromator[d] bandwidth ΔE (eV)	photons[c] / sec·mA·mrad·10% bandwidth (10^9)
32	0.112[a]	0.5	0.008	2.0
50	0.079[a]	1.6	0.02	3.9
70	0.062[a]	2.7	0.04	4.8
90	0.060[a]	4.0	0.07	5.6
110	0.070[a]	5.7	0.10	6.5
130	0.067[a]	7.6	0.14	7.3
150	0.060[a]	9.0	0.18	7.5
170	0.05[b]	8.6	0.23	6.3
190	0.05[b]	6.4	0.29	4.2
210	0.05[b]	5.7	0.35	3.4
230	0.05[b]	4.9	0.42	2.6
250	0.05[b]	4.4	0.50	2.2
270	0.05[b]	3.5	0.60	1.6
290	0.05[b]	0.8	0.70	0.3

a) See reference 5.
b) In lack of measured values for the quantum efficiency above 155 eV we have assumed a constant value of 0.05.
c) See reference 6.
d) Calculated according to Equation (1).

REFERENCES

1. Perlman, M. L., Rowe, E. M., Watson, R. E., Physics Today, July 1974, p. 30.
2. Winick, H. in Vacuum Ultraviolet Radiation Physics, (ed. Koch, E. E., Haensel, R., and Kunz, C.) Pergamon, Vieweg 1974, p. 776.
3. Brown, F. C., Bachrach, R. Z., Hagström, S. B. M., Lien, N., and Pruett, C. H., in Ref. 2, p. 785.
4. Saloman, E. B. and Ederer, D. L., Applied Optics <u>14</u>, 1029 (1975).
5. National Bureau of Standards (NBS) Report of Calibration for our diode in the range 10 eV $\leqslant h\nu \leqslant$ 66 eV (unpublished). Above 66 eV we used the values of Gudat, W., Kunz, G., and Lenth, W., in Ref. 2, p. 725, which were normalized to the NBS calibration values at 50 and 60 eV.
6. During the course of our measurements SPEAR operated at 3.3 GeV and ∿30 mA. The grasshopper monochromator utilizes about 2mrad of radiation. Thus the actual flux (photons/sec) was about a factor of 60 higher than the values listed in column 3 of Table I.
7. Here we have assumed a constant 0.1 Å bandpass (see Ref. 3). Then the relation $\Delta\lambda/\lambda = \Delta E/E$ yields equation (1).
8. Cooper, J. W., Phys. Rev. Lett. <u>13</u>, 762 (1964); Fano, U. and Cooper, J. W., Rev. Mod. Phys. <u>40</u>, 441 (1968).
9. Wehner, P. S., Stöhr, J., Apai, G., McFeely, F. R., Williams, R. S., Shirley, D. A., Phys. Rev. <u>B14</u>, 2411 (1976).
10. Stöhr, J., Apai, G., Wehner, P. S., McFeely, F. R., Williams, R. S., and Shirley, D. A., Phys. Rev. <u>B14</u>, 5144 (1976).
11. Haensel, R., Kunz, G., Sasaki, T., Sonntag, B., Applied Physics <u>7</u>, 301 (1968); Brown, F. C., Solid State Physics <u>29</u>, 1 (1974).

12. Lindau, I., Pianetta, P., Yu, K. Y., and Spicer, W. E. (Phys. Rev. B13, 492 (1976)) observed valence band peak modulations for Au in the range > 100 eV. However, we believe that these effects cannot solely be explained by atomic cross section effects but are more complex as discussed in Ref. 10.

13. See for example, Eastman, D. E. in Ref. 2, p. 417, and references therein.

14. See for example, Wertheim, G. K., Buchanan, D.N.E., Smith, N. V., and Traum, M. M.. Phys. Lett. A49, 191 (1974) and references therein.

15. Stöhr, J., McFeely, F. R., Apai, G., Wehner, P. S., and Shirley, D.A., Phys. Rev. B14, 4431 (1976).

16. See for example, Pincherle, L., Electronic Energy Bands in Solids, MacDonald, London, 1971, pp. 104-108.

17. Smith, N. V., Phys. Rev. B3, 1862 (1971).

18. Hodges, L., Ehrenreich, H., and Lang, N. D., Phys. Rev. 152, 505 (1966).

19. Feibelman, P. J. and Eastman, D. E., Phys. Rev. B10, 4932 (1974).

20. Feuerbacher, B. and Willis, R. F., J. Phys. C 9, 169 (1976).

21. Lindau, I. and Spicer, W. E., J. Electron Spectroscopy 3, 409 (1974).

22. Penn, D. R., J. Electron Spectroscopy 9, 29 (1976).

23. Janak, J. F., Williams, A. R., and Moruzzi, V. L., Phys. Rev. B11, 1522 (1975).

24. Wagner, L. F., Hussain, Z., and Fadley, C. S., Solid State Commun. 21, 257 (1977).

25. Stöhr, J., Wehner, P. S., Williams, R. S., Apai, G., and Shirley, D. A. (to be published).

26. Dietz, E., Becker, H., and Gerhardt, U., Phys. Rev. Lett. 36, 1397 (1976); Rowe, J. E., Margaritondo, G., and Kasper, H., Nuovo Cimento 38B, 226 (1977); Knapp, J. A. and Lapeyre, G. J., Nuovo Cimento 39B, 696 (1977).

27. Burdick, G. A., Phys. Rev. 129, 138 (1963).

28. Mahan, G. D., Phys. Rev. B2, 4334 (1970).

29. Williams, R. S., Wehner, P. S., Stöhr, J., and Shirley, D. A. (to be published).

30. Shevchik, N. J., private communication, 1977.

31. Williams, R. S., Wehner, P. S., Stöhr, J., and Shirley, D. A., Phys. Rev. Lett. XX, XXX (1977).

32. Warren, B. E., X-ray Diffraction, Addison-Wesley, 1969, p. 159-169.

33. International Tables for X-ray Crystallography (ed. McGillavry, Rieck, G. D., and Lonsdale, K.), The Kynoch Press, Birmingham, England 1962, p. 237.

34. Wallis, R. F., Clark, B. C., and Herman, R., Phys. Rev. 167, 652 (1968).

35. Cheng, D. J., Wallis, R. F., Megerle, G., and Somorjai, G. A., Phys. Rev. B12, 5599 (1975).

36. Nicklow, R. M., Gilat, G., Smith, H. G., Raubenheimer, L. J. and Wilkinson, M. K., Phys. Rev. 164, 922 (1967).

37. Baird, R. J., Wagner, L. F., and Fadley, C. S., Phys. Rev. Lett. 37, 111 (1976).

38. Stöhr, J., Wehner, P. S., and Apai, G., unpublished results.

39. Wehner, P. S., Stöhr, J., Apai, G., McFeely, F. R., and Shirley, D. A., Phys. Rev. Lett. 38, 169 (1977).

40. Apai, G., Wehner, P. S., Stöhr, J., Williams, R. S., and Shirley, D. A., Solid State Commun. 20, 1141 (1976).

41. Gustafsson, T., Plummer, E. W., Eastman, D. E., and Freeouf, J. L., Solid State Commun. 17, 391 (1975).

42. Rabalais, J. W., Debies, T. P., Berkosky, J. L., Huang, J. J., and Ellison, F. O., J. Chem. Phys. 61, 516 (1974).

43. Morgan, A. E. and Somorjai, G. A., J. Chem. Phys. 51, 3309 (1969).

44. See Ref. 17. Smith's d-block parameters were used unchanged. The plane-wave (PW) and d-PW hybridization parameters were changed as follows: $\alpha = 0.014$, $V_{200} = 0.0082$, $V_{111} = -0.0071$, $B_1 = 0.4$, $B_2 = B_3 = 1.49$, $\beta = -0.06$ and a spin-orbit parameter $\xi = 0.038$ Ry.

45. Desjonquères, M. C. and Cyrot-Lackmann, F., Solid State Commun. 18, 1127 (1976).

46. Davenport, J. W., Phys. Rev. Lett. 36, 945 (1976).

47. Turner, D. W., Baker, C., Baker, A. D., and Brundle, C. R., Molecular Photoelectron Spectroscopy, Wiley-Interscience, London (1970), p. 49.

48. Batra, I. P. and Bagus, P. S., Solid State Commun. 16, 1097 (1975).

49. Bagus, P. S. and Herman, K., Surface Science (to be published).

50. Williams, P. M., Butcher, P., Wood, J., and Jacobi, K., Phys. Rev. B14, 3215 (1976).

51. Lloyd, D. R., Quinn, C. M., and Richardson, N. V., Solid State Commun. 20, 409 (1976).

52. Apai, G., Wehner, P. S., Williams, R. S., Stöhr, J., and Shirley, D. A., Phys. Rev. Lett. 37, 1497 (1976).

53. Duke, C. B. in Advances in Chemical Physics, Vol. XXVII edited by Prigogine, I. and Rice, S. A. (Interscience).

54. Tracy, J. C., Journal of Chem. Phys. 56, 2736 (1972).

55. Liebsch, A., Phys. Rev. Lett. 32, 1203 (1974); Liebsch, A., Phys. Rev. B15, 544 (1976).

56. Tong, S. Y. and Van Hove, M. A., Solid State Commun. 19, 543 (1976) and references therein.

57. Dill, D., Siegel, J., and Dehmer, J. L., J. Chem. Phys. 65, 3158 (1976).

58. Allyn, C. L., Gustafsson, T., and Plummer, E. W., Chem. Phys. Lett. 47, 127 (1977).

FIGURE CAPTIONS

Fig. 1 a) Schematic illustration of an NBS-Al_2O_3 photodiode.

b) Transmission function of the monochromator located on the 4° port on Beam Line I at SSRP measured as the photocurrent from an NBS-Al_2O_3 photodiode. To obtain the absolute flux out of the monochromator, the curve must be corrected by the quantum efficiency of Al_2O_3 in this energy range.

Fig. 2 Quantum efficiency of Al_2O_3 in the photon energy range 10-160 eV (cf. Ref. 5).

Fig. 3 Spectral distribution of synchrotron radiation emitted from the storage ring SPEAR as a function of the electron beam energy.

Fig. 4 Relative d-band intensity of Cu, Ag, and Au as a function of photon energy. Curves have been corrected for the collecting efficiency of the cylindrical mirror analyzer, the transmission of the monochromator, and inelastic background.

Fig. 5 Photoemission spectra of polycrystalline Ag valence bands. Experimental resolution was 0.35 eV for the spectra between 60 eV $\leqslant h\nu \leqslant$ 150 eV and 0.6 eV at 1487 eV. No correction has been made for inelastic background.

Fig. 6 Schematic illustration of the effect of the total Ag 4d photoemission cross section on the detailed shape of the Ag valence band spectrum at $h\nu \approx$ 120 eV. The higher binding energy peak is predicted to have a 20% higher cross section than the lower binding energy peak and thus increase in relative intensity.

Fig. 7 Valence band photoemission spectra obtained from polycrystalline Cu for a series of photon energies. Experimental resolution was 0.35 eV for the spectra between 40 and 200 eV and 0.6 eV for the XPS spectrum. No correction for inelastic background has been made.

Fig. 8 Photoelectron mean free path in Cu as a function of kinetic energy. The values between 30 and 100 eV were obtained from Ref. 21 and those above 200 eV from Ref. 22. The region between 100 and 200 eV is shown as a dashed line because no experimental or theoretical results are available in this region.

Fig. 9 a) PED's calculated for Cu assuming strict $\vec{k}$ and energy ($E_f(\vec{k}) - E_i(\vec{k}) - h\nu \leqslant 0.1$ eV) conservation. The calculated curves are convoluted with a 0.5 eV FWHM Gaussian function. b) Experimental results for polycrystalline Cu. The original data in Fig. 7 have been corrected for inelastic background. c) PED's, convoluted with 0.5 eV FWHM Gaussian function, calculated for Cu assuming an uncertainty in the final state momentum. The amount of uncertainty $|\vec{\Delta}|$ is in units of $2\pi/a$ where a (3.615 Å) is the lattice constant of Cu. The theoretical density of states (DOS) is shown at the top of column c.

Fig. 10 Photoemission spectra obtained from the three low-index crystal faces of Cu using angle-resolved normal photoemission; a) (001); b) (110); c) (110). The angular resolution was ∿±5° and the energy resolution was $\leqslant 0.2$ eV.

Fig. 11 a) (010) projection of the three-dimensional Brillouin Zone (BZ) of a fcc lattice.

b) Photoemission at hν ≈ 150 eV along the [001] direction assuming an angular resolution of ±5° and free electron final states. Only a small fraction of the first BZ (a section of a spherical surface) can give rise to photoemission ($\vec{q}$ vectors) into the detector due to momentum conservation.

c) Photoemission at hν ≈ 150 eV along the [001] direction assuming an uncertainty in the final state momentum ($\vec{q}$) of ∿15% of 2π/a. All states in the dashed area can give rise to photoemission into the detector due to the uncertainty in $|\vec{q}|$.

Fig. 12 Comparison of a calculation (dashed curve) for photoemission in the [110] direction at a photon energy of 45 eV and an angular resolution of ±5° to the experimentally observed spectrum (solid line). The calculation was convoluted with a 0.5 eV FWHM Gaussian function to simulate experimental resolution.

Fig. 13 Comparison of experimental peak positions with Burdick's band structure of Cu [27] for the three directions investigated. The inset at the top of each panel shows the propagation direction of the photoelectron in the extended zone scheme. The bottom inset establishes a correspondence between photon energy and the part of the Brillouin Zone sampled; a) Cu[001]; b) Cu[110]; c) Cu[111]. Note different scales.

Fig. 14 Relative area under the band 6 peak compared to the total Cu valence band area (as a function of the emission angle measured from the sample normal) for $h\nu = 45$ eV. The azimuthal orientation of the crystalline axes defining the detection plane for the data presented in Fig. 14a and c were equivalent to Fig. 14b and d (insets), respectively. The angular acceptance was ±5° and the energy resolution 0.2 eV.

Fig. 15 Temperature dependence of the angle-resolved normal photoemission spectrum from a Cu(110) crystal at $h\nu = 45$ eV. The angular resolution was ±5°.

Fig. 16 a) Experimental intensity of the peak at $\sim$0.5 eV binding energy in Fig. 15 as a function of temperature (full circles connected by a dashed line) as compared to the Debye-Waller factor f^n (solid lines). The different curves for f^n correspond to calculations assuming a mean-square displacement of n times the bulk value.

b) Ratio of indirect to direct transitions as derived from the spectra in Fig. 15 versus temperature. For the data points shown as squares and triangles we have assumed that at room temperature the main d-band peak is composed of 100% and 85% direct transitions, respectively.

Fig. 17 Photoemission spectra of clean Pt(111) and Pt(111) + 5L CO in the energy range $40 \text{ eV} \leqslant h\nu \leqslant 150$ eV. Experimental resolution was 0.8 eV. Note increase in the intensity of the CO derived peaks (at $\sim$8.7 eV and 11.8 eV E_B) as $h\nu$ is increased to 150 eV.

Fig. 18 Relative intensity of the ($5\sigma + 1\pi$) CO peak at ∿8.7 eV E_B to the Pt valence band intensity as a function of photon energy.

Fig. 19 Plot of the theoretical CO ($5\sigma + 1\pi$) cross section from Ref. 42 and the experimental Pt valence band intensity (Ref. 40). The resultant ratio is plotted as a function of photon energy in the insert on a linear scale.

Fig. 20 The experimental results from Ref. 41 for the ratio of the CO peak ($5\sigma + 1\pi$) with respect to the Ni VB and Pd VB (triangles) are compared with the ratio formed from the theoretical $5\sigma + 1\pi$ cross sections from Ref. 42 and the experimental cross sections for Cu VB and Ag VB presented in Section 3.1 (solid curves).

Fig. 21 The relative cross section of the Ag VB (Ref. 9) and the CO $5\sigma + 1\pi$ molecular orbitals (Ref. 42) in the photon energy range $40 \text{ eV} \leqslant h\nu \leqslant 180 \text{ eV}$. The resultant ratio is plotted as a function of photon energy in the insert on a linear scale.

Fig. 22 Photoemission spectra of CO adsorbed on Pt(111) at 70 eV and 150 eV photon energy. Note the enhancement of the CO derived peaks at $h\nu = 150$ eV as compared to 70 eV and the decrease in intensity of the Pt valence band near E_F at both energies.

Fig. 23 a) Angle-resolved photoemission spectra of clean Pt(111) and Pt(111) + 4L CO at an emission angle of 40° from the sample normal and for $h\nu = 40.8$ eV. The experimental resolution was 0.2 eV. Note the large decrease in emission from the Pt valence band peak near E_F and the splitting in the CO derived peak at 8.7 eV E_B.

b) Detailed experimental geometry for the spectra above. The angular resolution was ±5°.

Fig. 24 Total valence band density of states and the t_{2g} and e_g projections for Pt calculated using a tight-binding interpolation scheme as discussed in Ref. 44. The density of states histograms were convoluted with a 0.5 eV FWHM Gaussian function.

Fig. 25 Angle-resolved photoemission spectra of Pt(111) + 4L CO at $h\nu = 40.8$ eV as a function of the angle Θ between the surface normal and the photoelectron propagation direction. The experimental resolution was 0.2 eV. The experimental geometry is that shown in Fig. 23b.

Fig. 26 a) Experimental arrangement of the photon beam and detector with respect to the crystal normal. Θ is defined positive for clockwise rotation, negative for counterclockwise rotation of the crystal normal with respect to the fixed photoelectron propagation direction into the analyzer.

b) Experimental orientation of the Ni and Pt crystals in the (111) plane.

c) Intensity ratio of the two CO derived peaks $4\sigma/(1\pi + 5\sigma)$ as a function of the angle Θ for CO adsorbed on Ni and Pt. Θ is defined in Fig. 26a.

d) Calculated intensity ratio $4\sigma/1\pi + 5\sigma)$, scaled to best fit experiment, for three orientations of the CO molecule with respect to the surface as a function of Θ. Θ is defined in Fig. 26a.

Fig. 27 Schematic illustration of two processes which may contribute to the photoemission process: 1) photoelectrons originating from the molecule and making a direct path of the detector, and 2) indirect emission after backscattering from the substrate.

Fig. 28 Comparison of experimental spectra of CO on Pt(111) using 150 eV and 40 eV synchrotron radiation and 40.8 eV HeII radiation as a function of the photoemission angle Θ, as defined in Fig. 29b and c. Note the strong variation in the CO peak intensity of A and B with a change in angle or photon energy.

Fig. 29 Plot of the measured intensity ratio $4\sigma/(1\pi + 5\sigma)$ for two different light sources (HeII and synchrotron) and photon energies ($\sim$40 eV and 150 eV). All spectra were taken in the same geometry as shown in Fig. 29b and c. The difference between the intensity ratio derived from HeII and synchrotron radiation spectra is due to the polarized nature of the synchrotron light. The dramatic inversion of the ratio $4\sigma/(1\pi + 5\sigma)$ between 40 eV and 150 eV may indicate the importance of final-state scattering effects.

Fig. 30 a) Integrated intensity from CO $(1\pi + 5\sigma)$ and CO 4σ adsorbate MO levels as a function of photon energy. The geometry is the same as described in Fig. 29b and c. The right hand panel shows the ratio for $4\sigma/(1\pi + 5\sigma)$ as a function of photon energy. Photoelectrons were measured at a normal emission angle.

b) Integrated intensity from CO (1π + 5σ) and CO 4σ adsorbate MO levels as a function of photon energy for a 45° electron take-off angle. The right hand panel shows the ratio similarly to Fig. 30a.

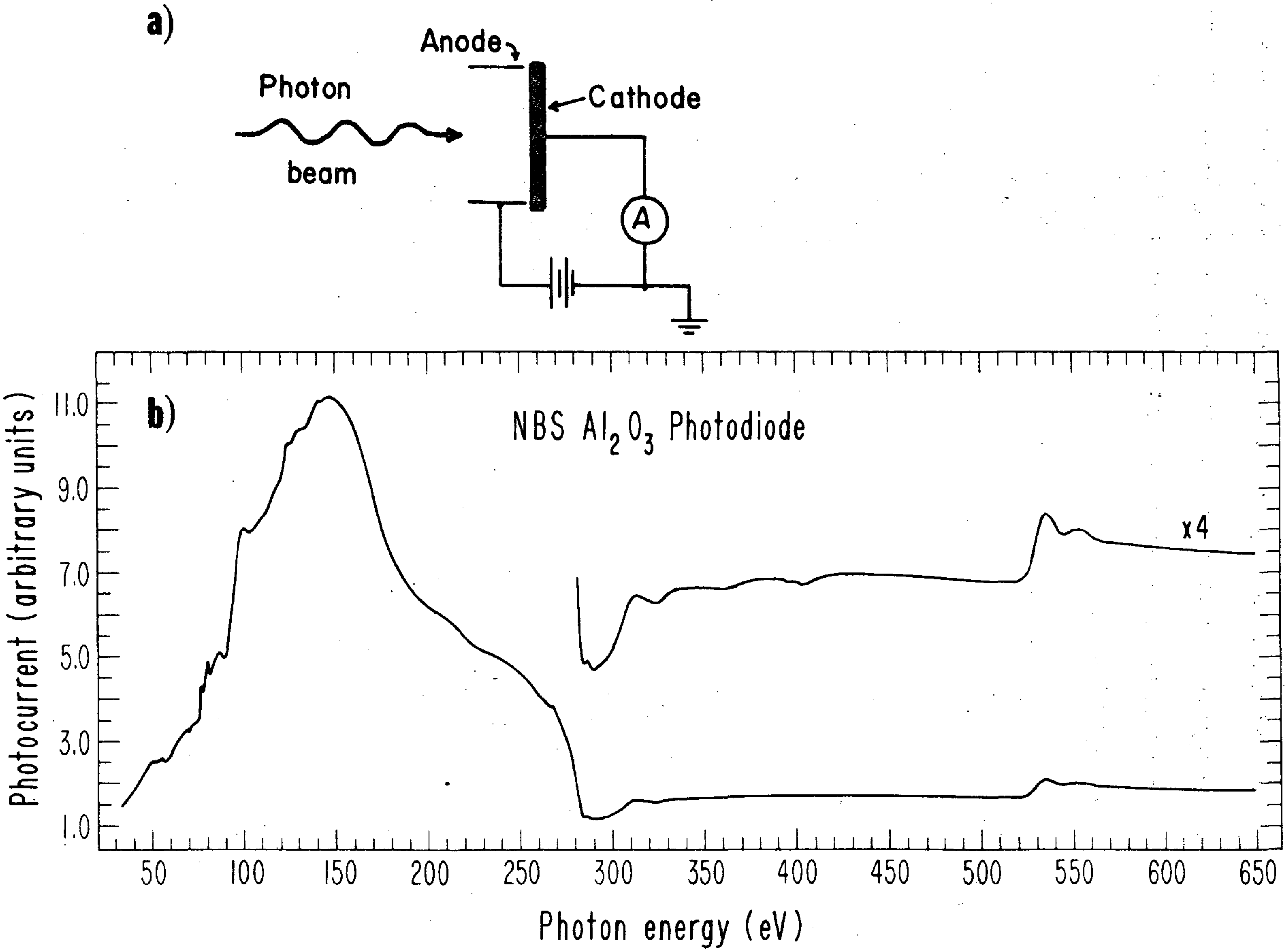

Fig. 1

XBL 775-8634

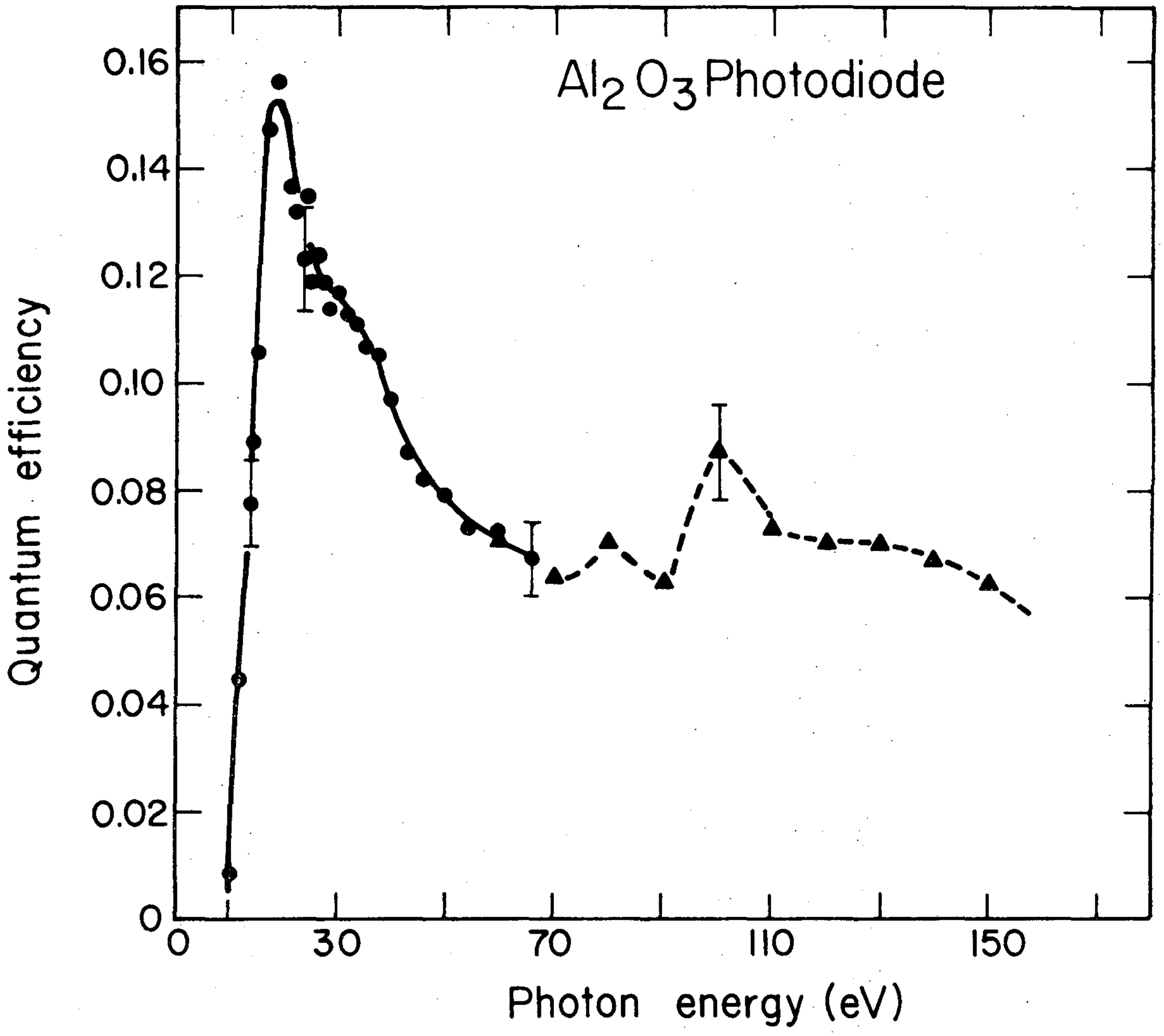

Fig. 2

XBL 775-1019

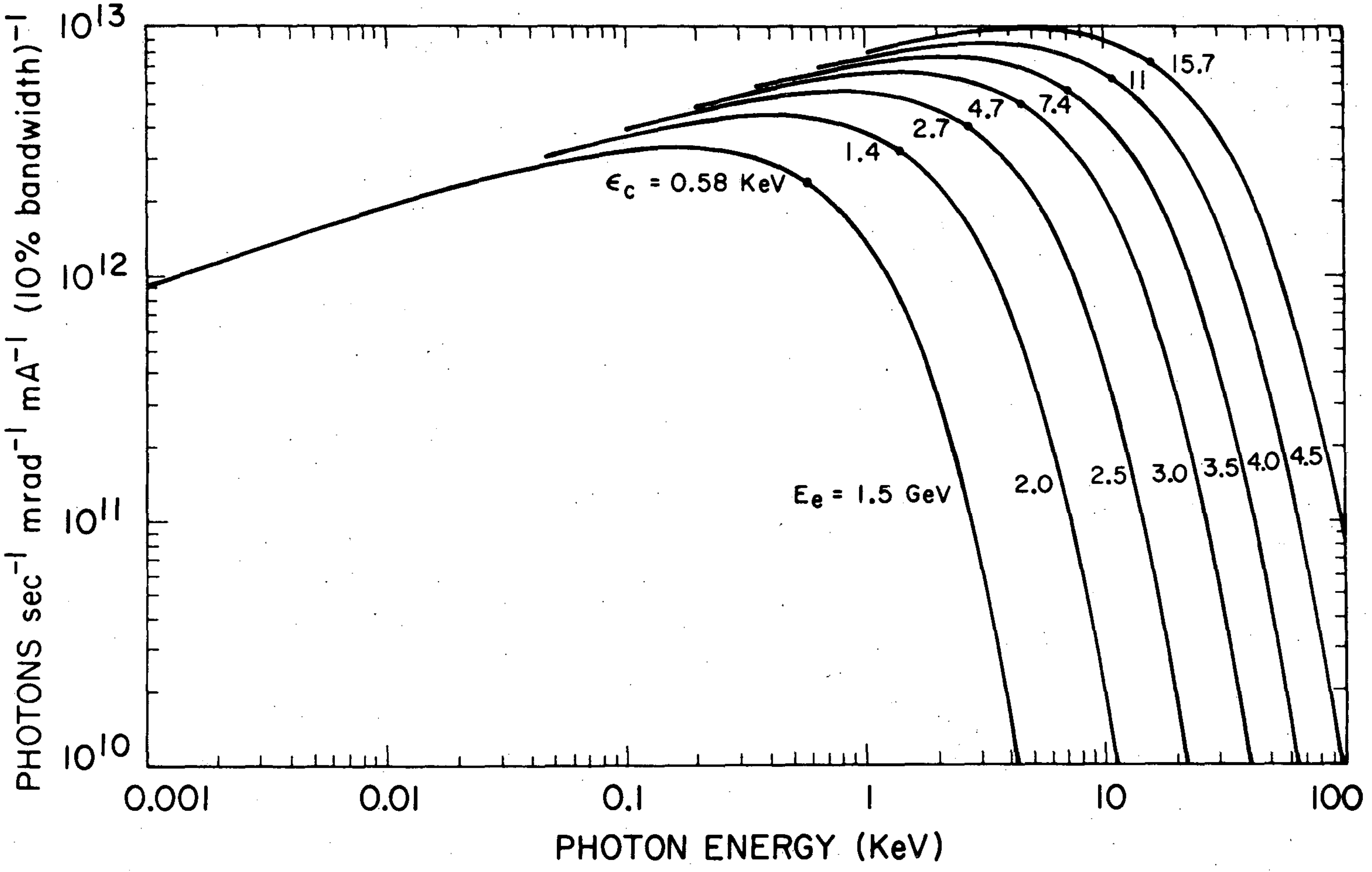

Fig. 3

XBL 776-9334

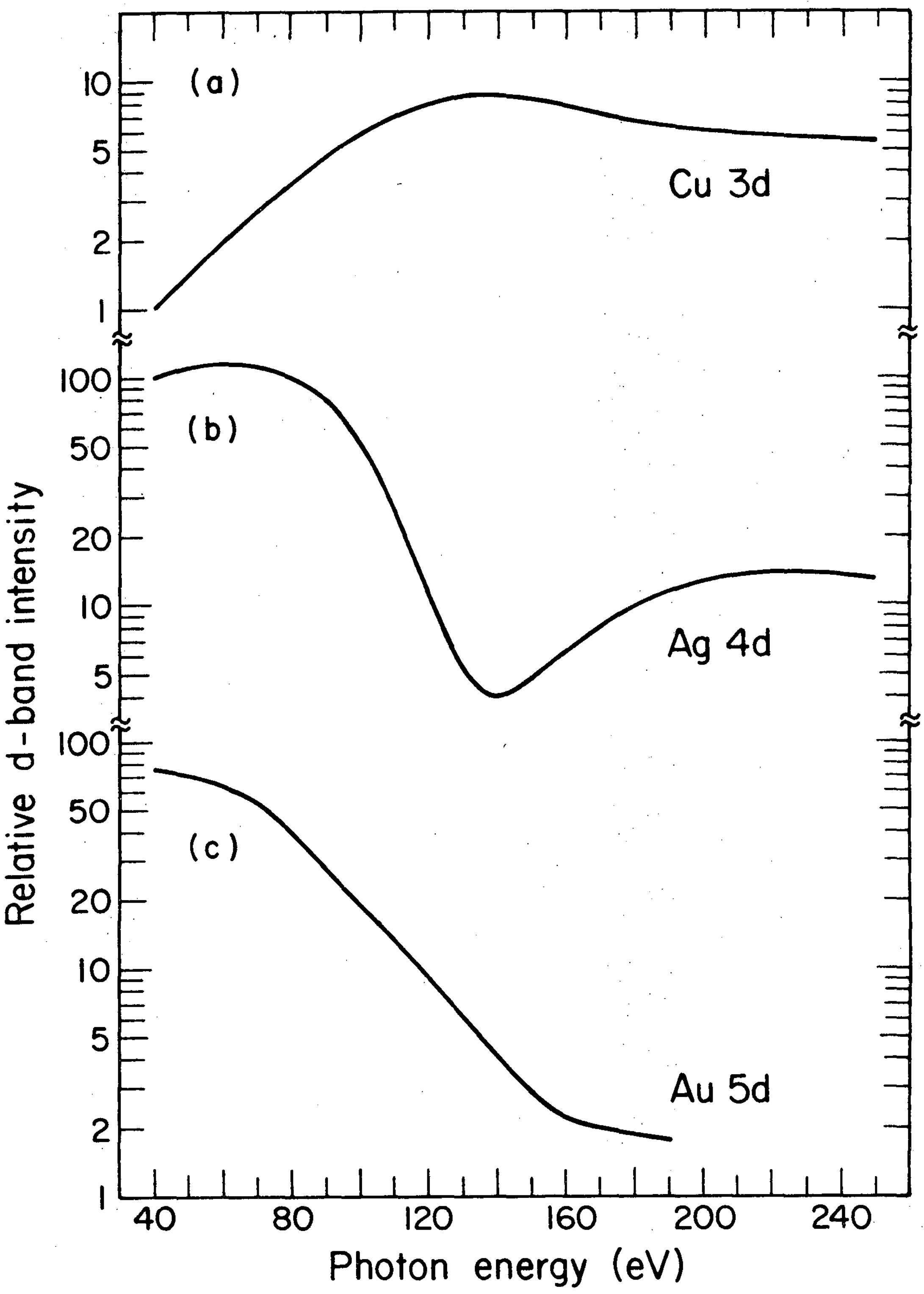

Fig. 4

XBL777-1372

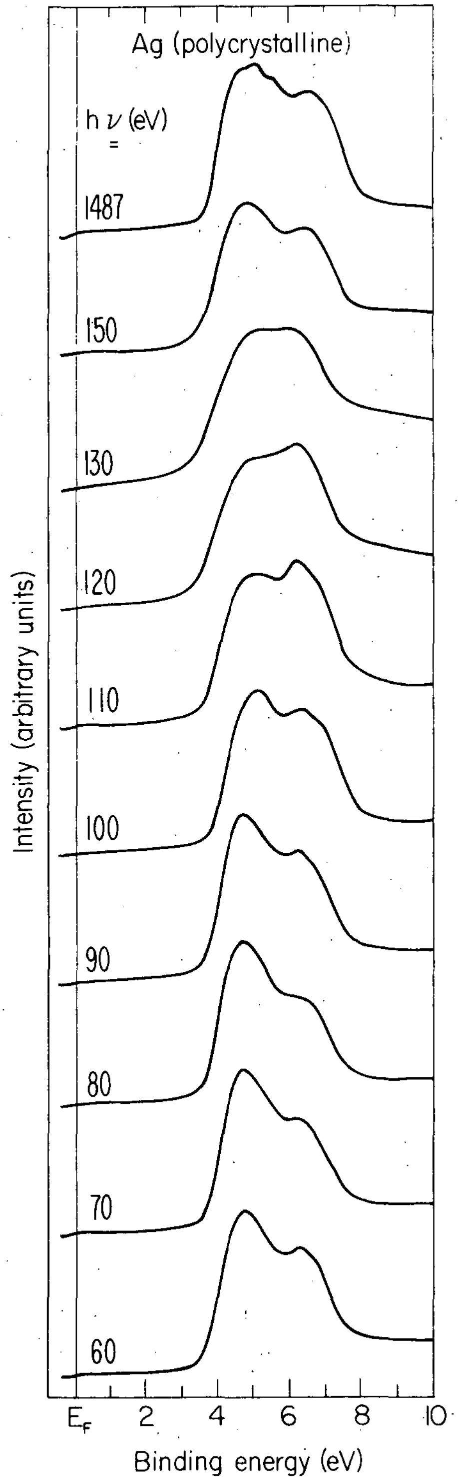
Ag (polycrystalline)
h ν (eV)
=
1487
150
130
120
110
100
90
80
70
60
Intensity (arbitrary units)
E_F
2
4
6
8
10
Binding energy (eV)
XBL 776-1240

Fig. 5

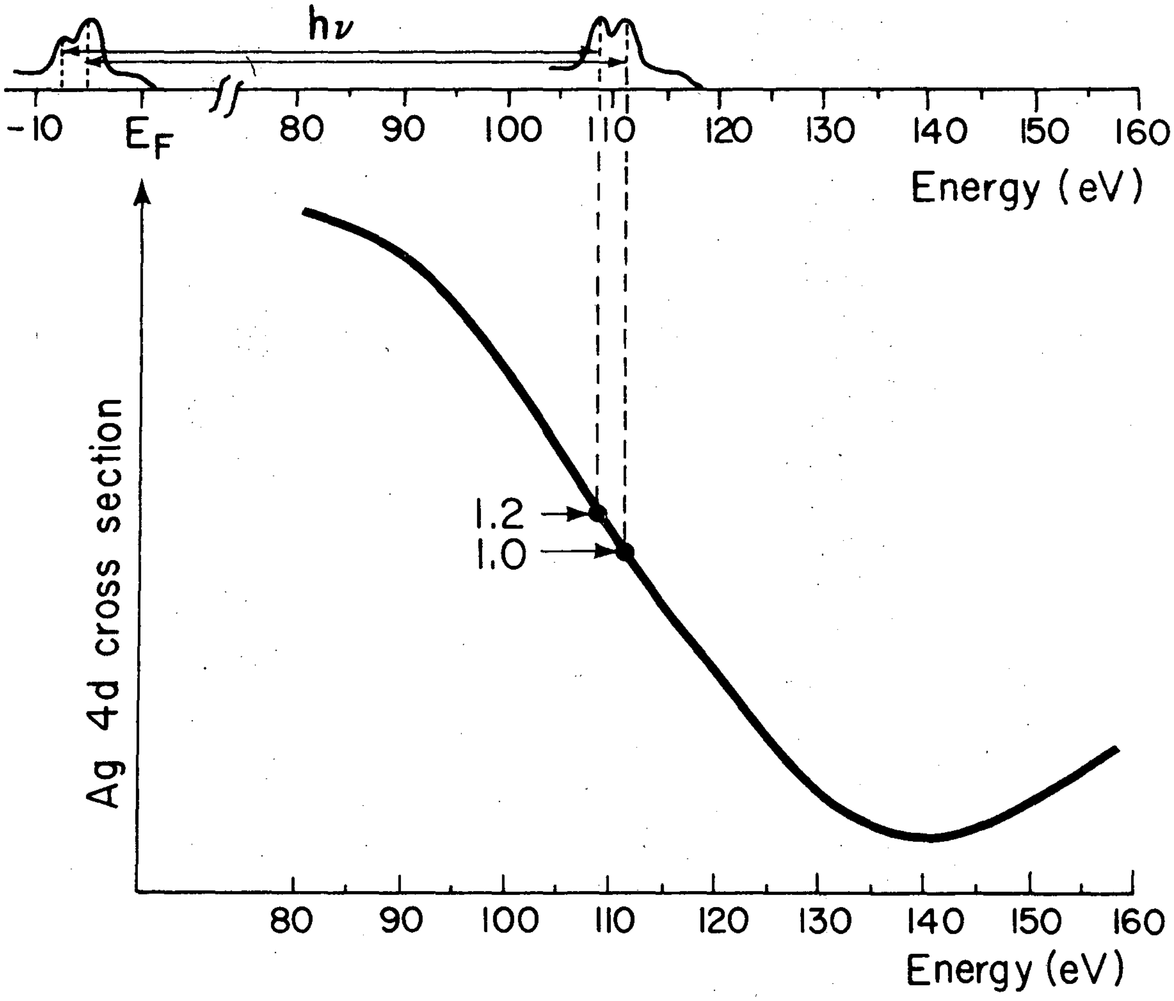

Fig. 6

XBL 775-1016

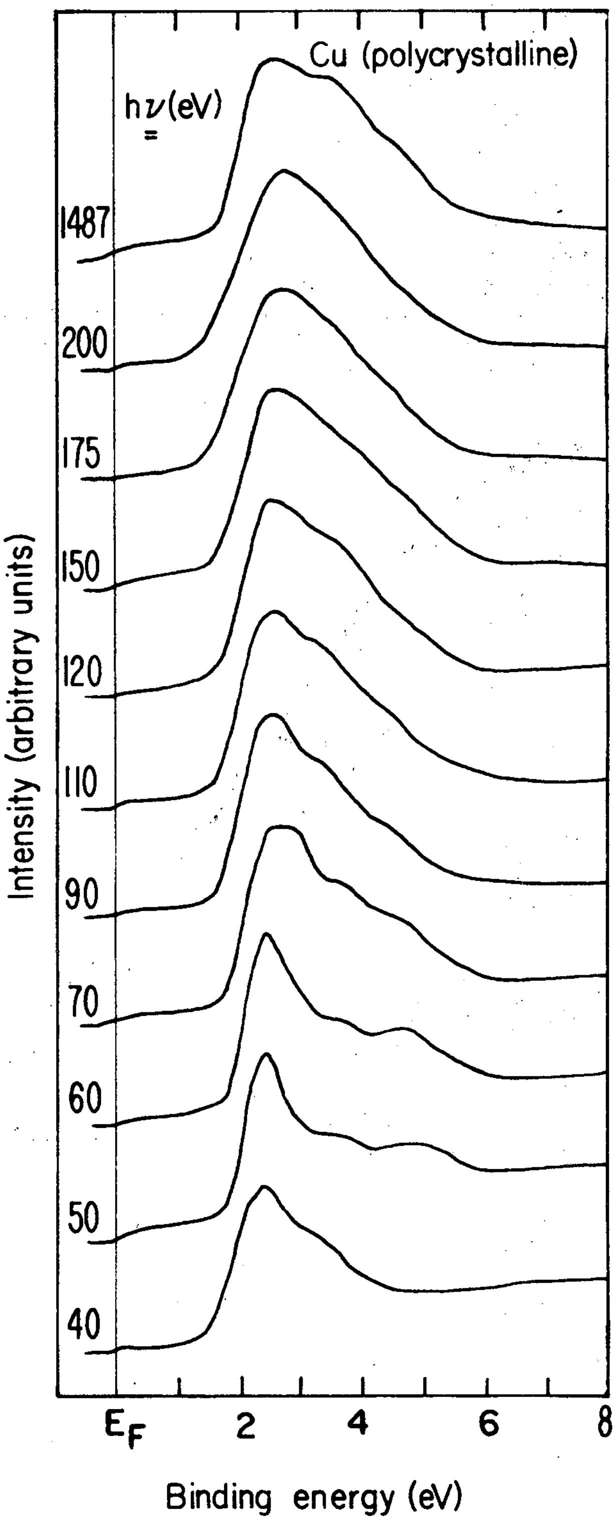

XBL 776-1239

Fig. 7

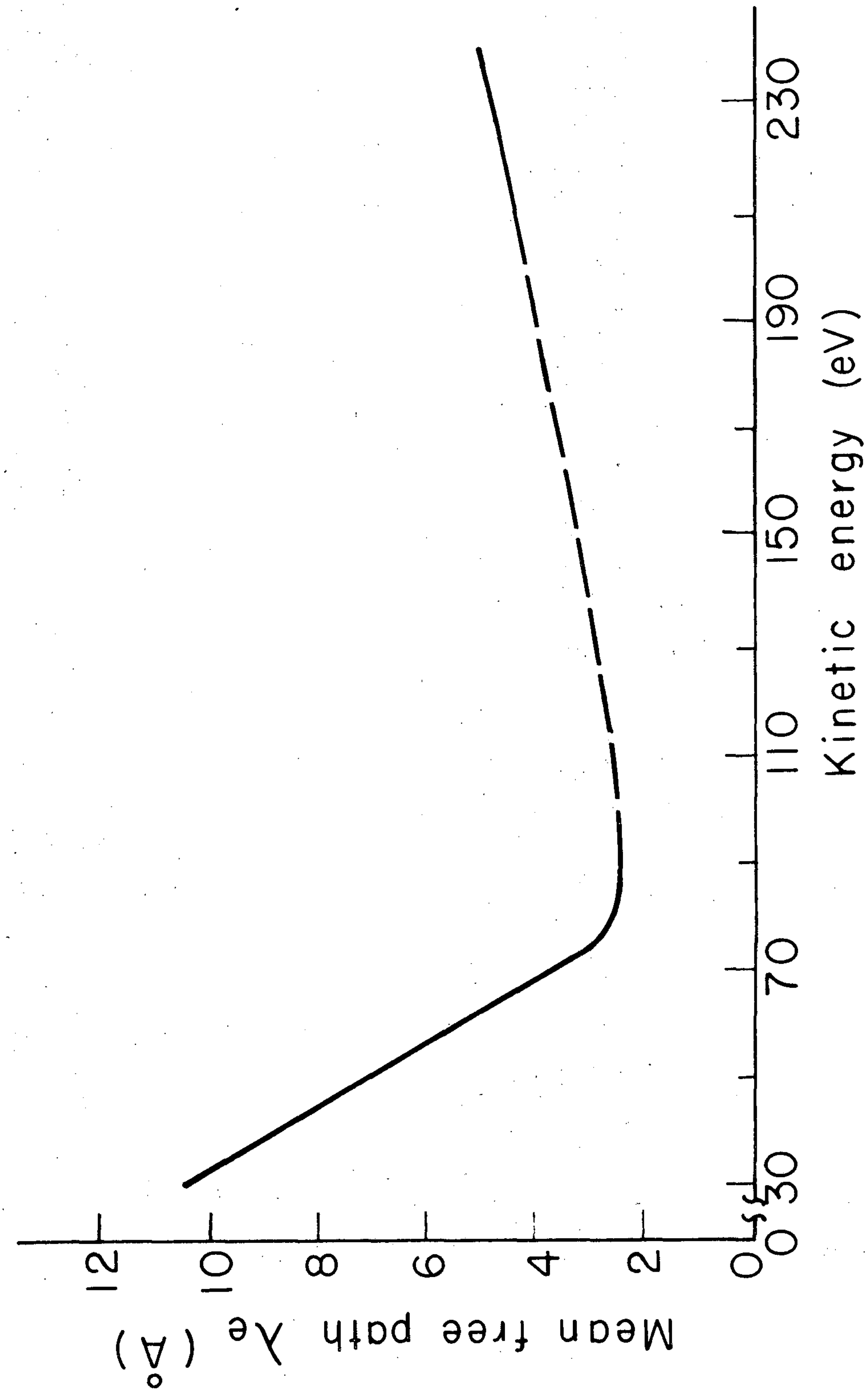

XBL777-1375

Fig. 8

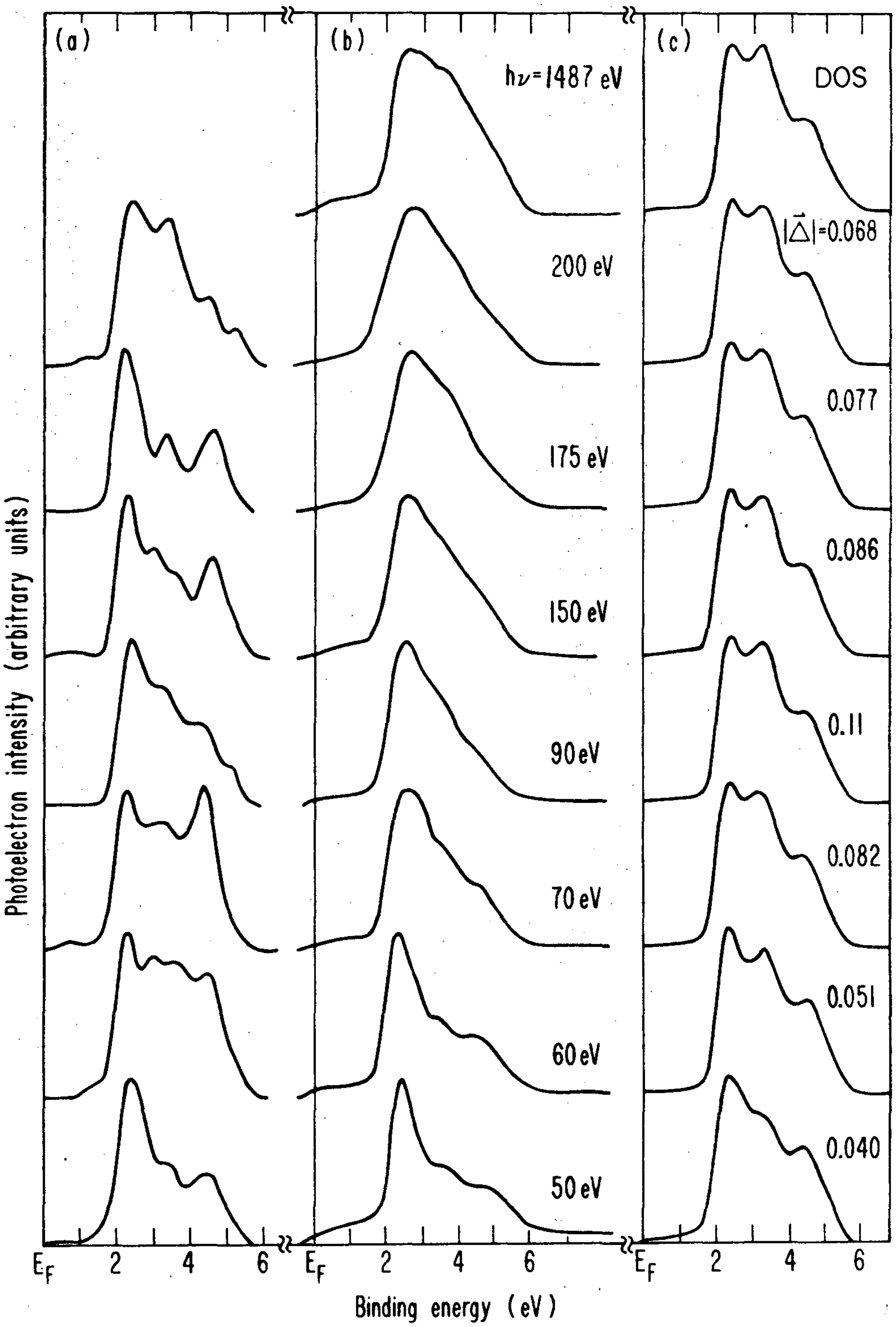

XBL 777-1371

Fig. 9

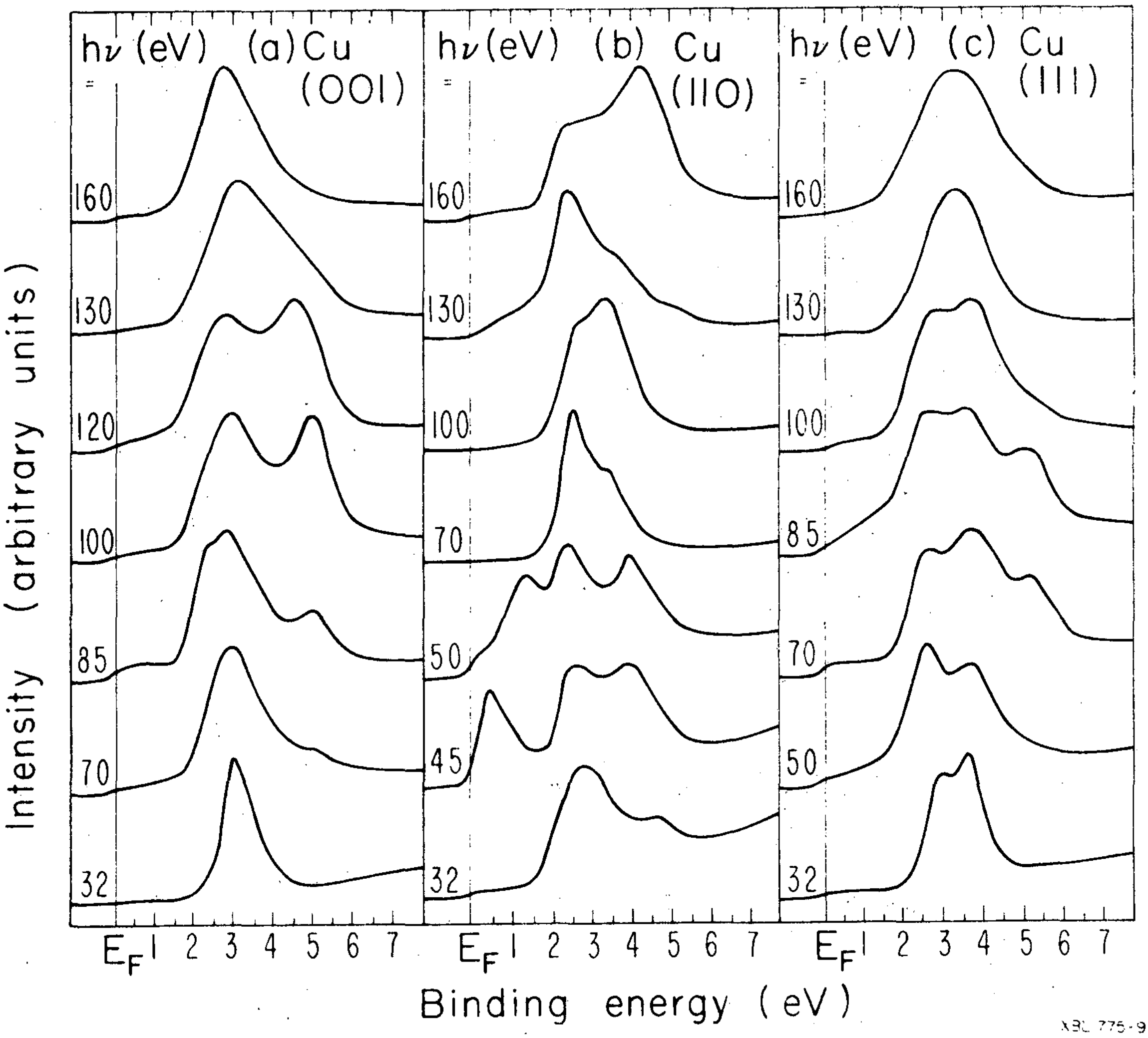

XBL 775-920

Fig. 10

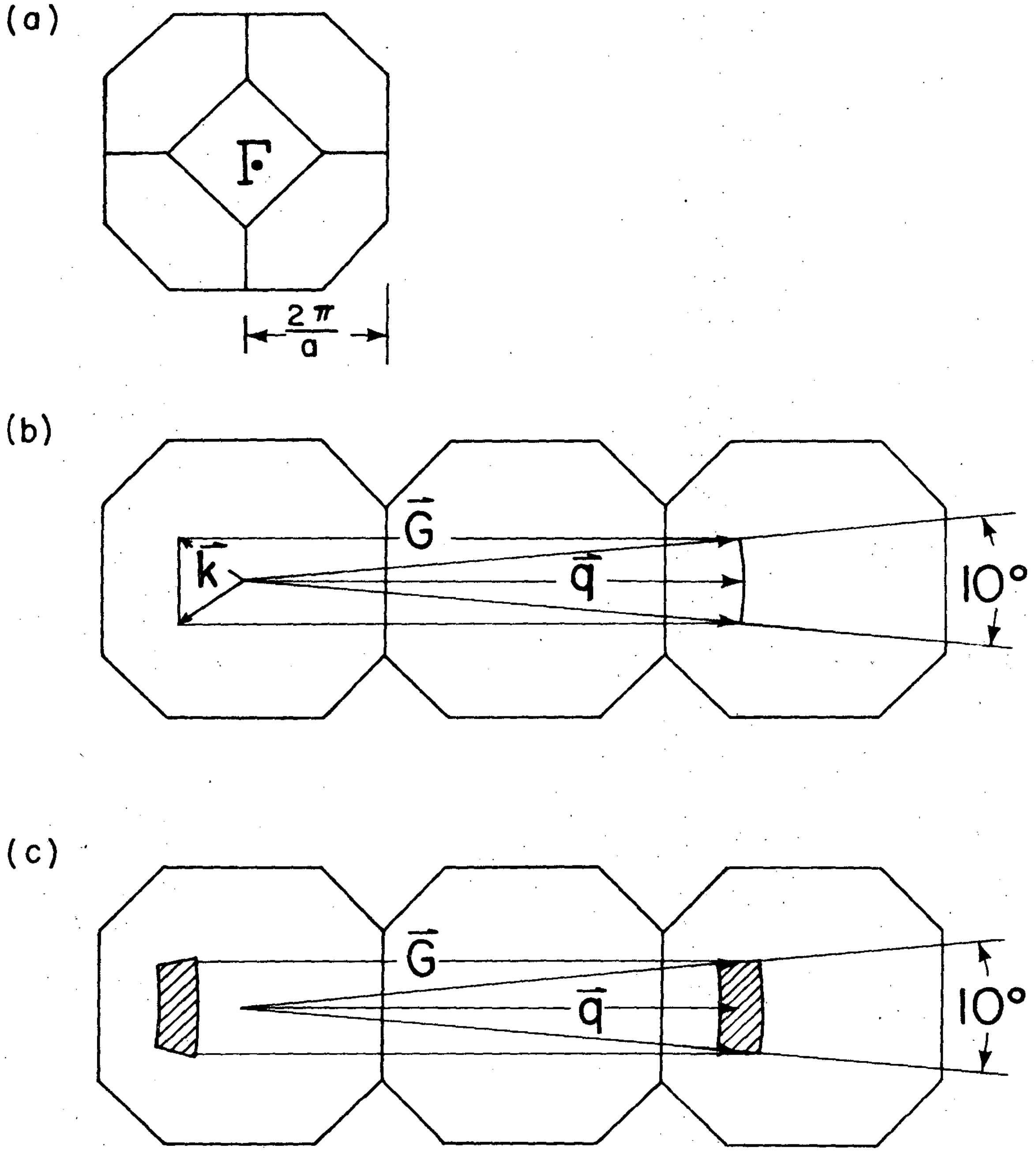

XBL 777-1373

Fig. 11

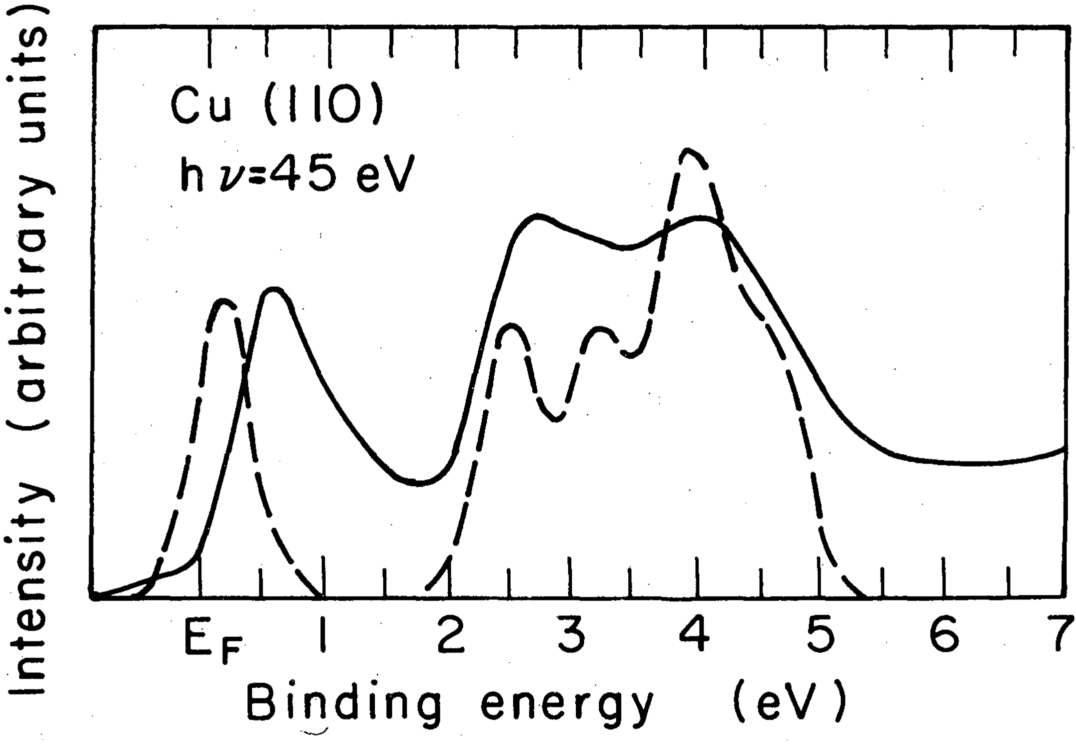

XBL 777-1374

Fig. 12

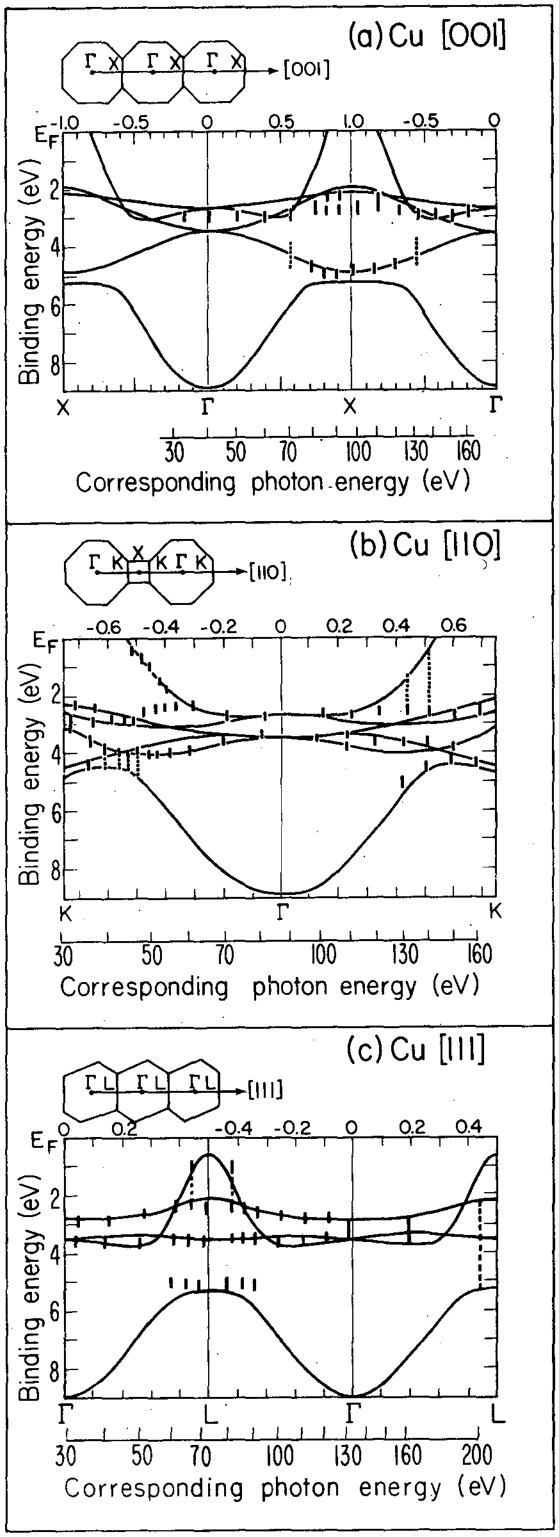

XBL 775-921

Fig. 13

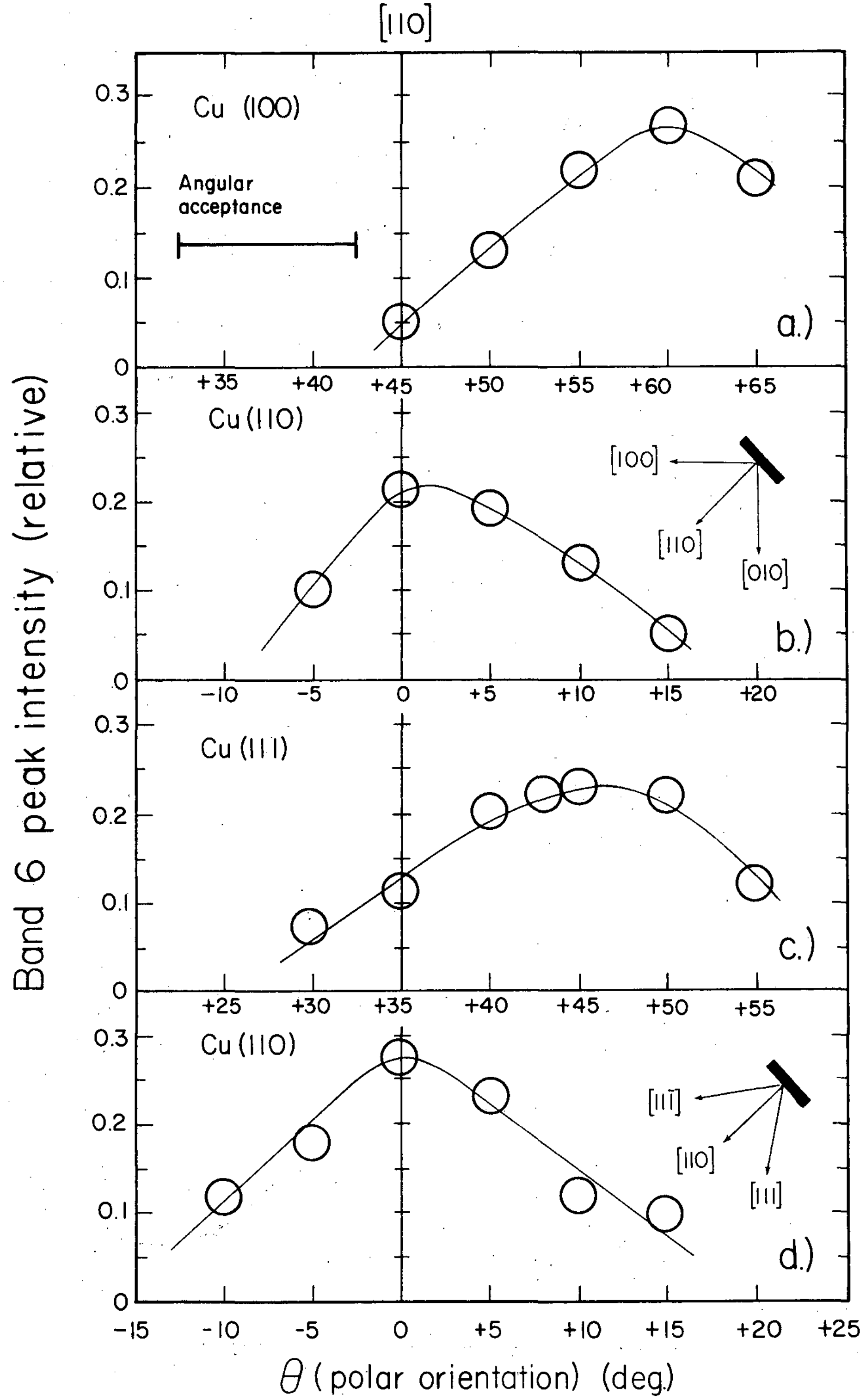

XBL775-1057

Fig. 14

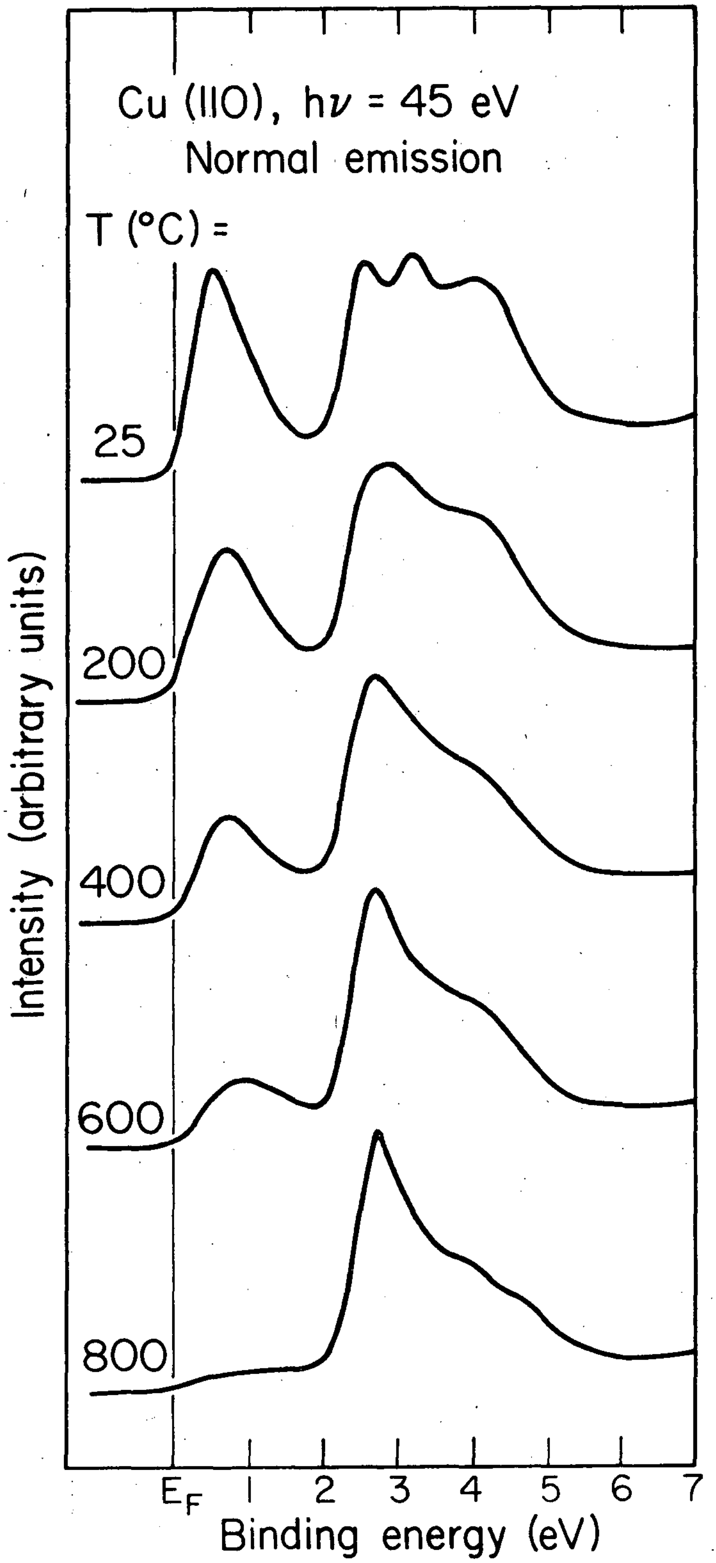

XBL 774-818

Fig. 15

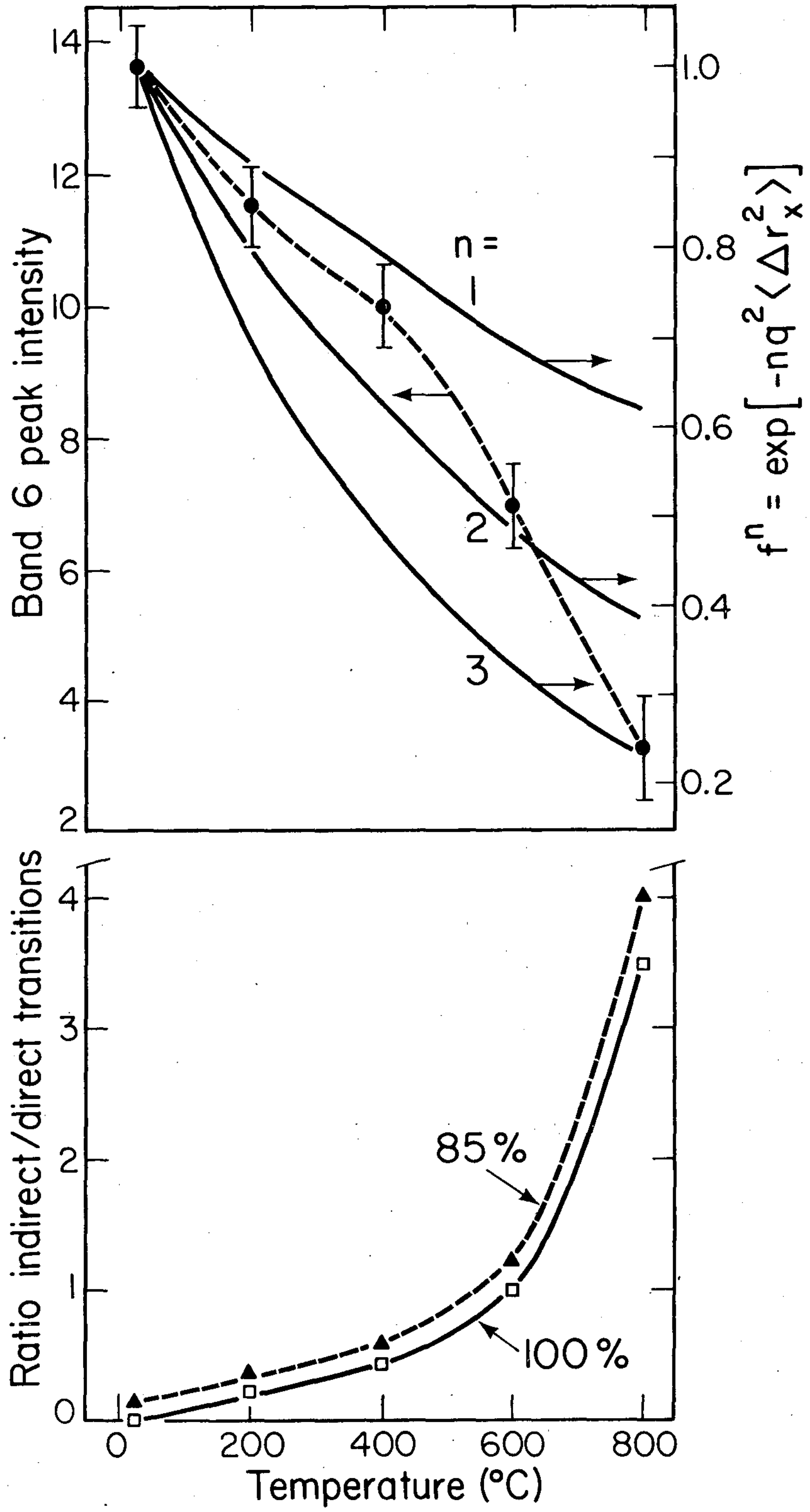

XBL 774-819

Fig. 16

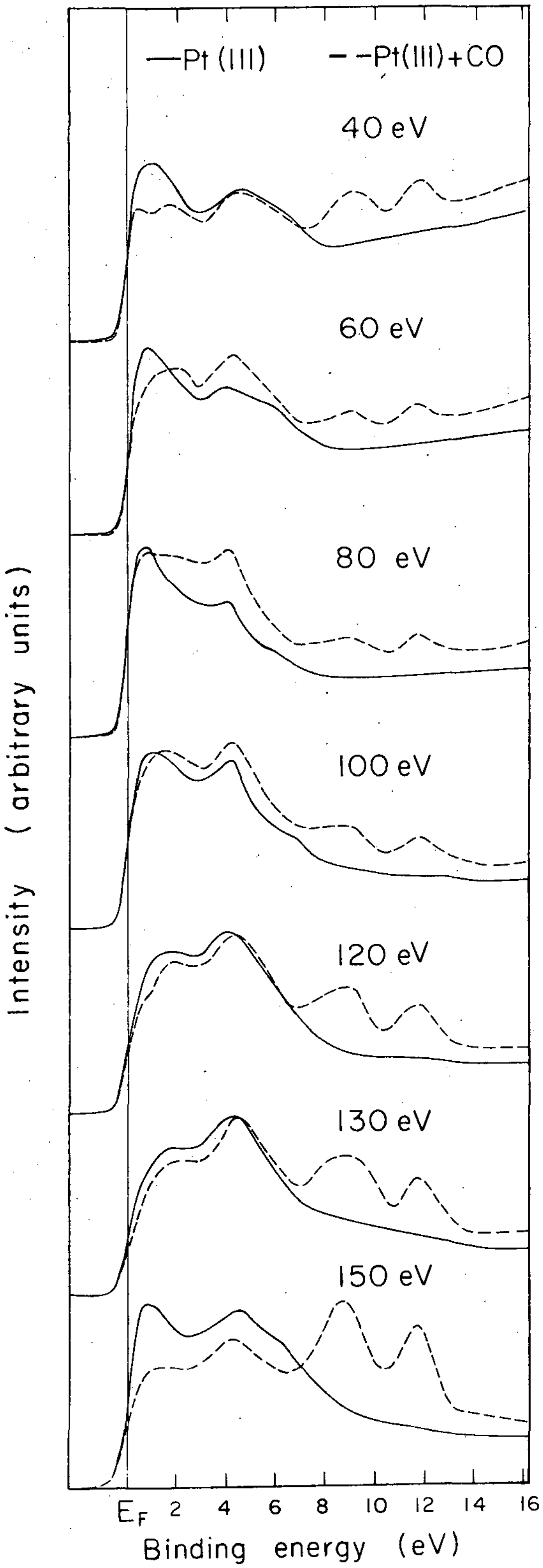

XBL 764-2733

Fig. 17

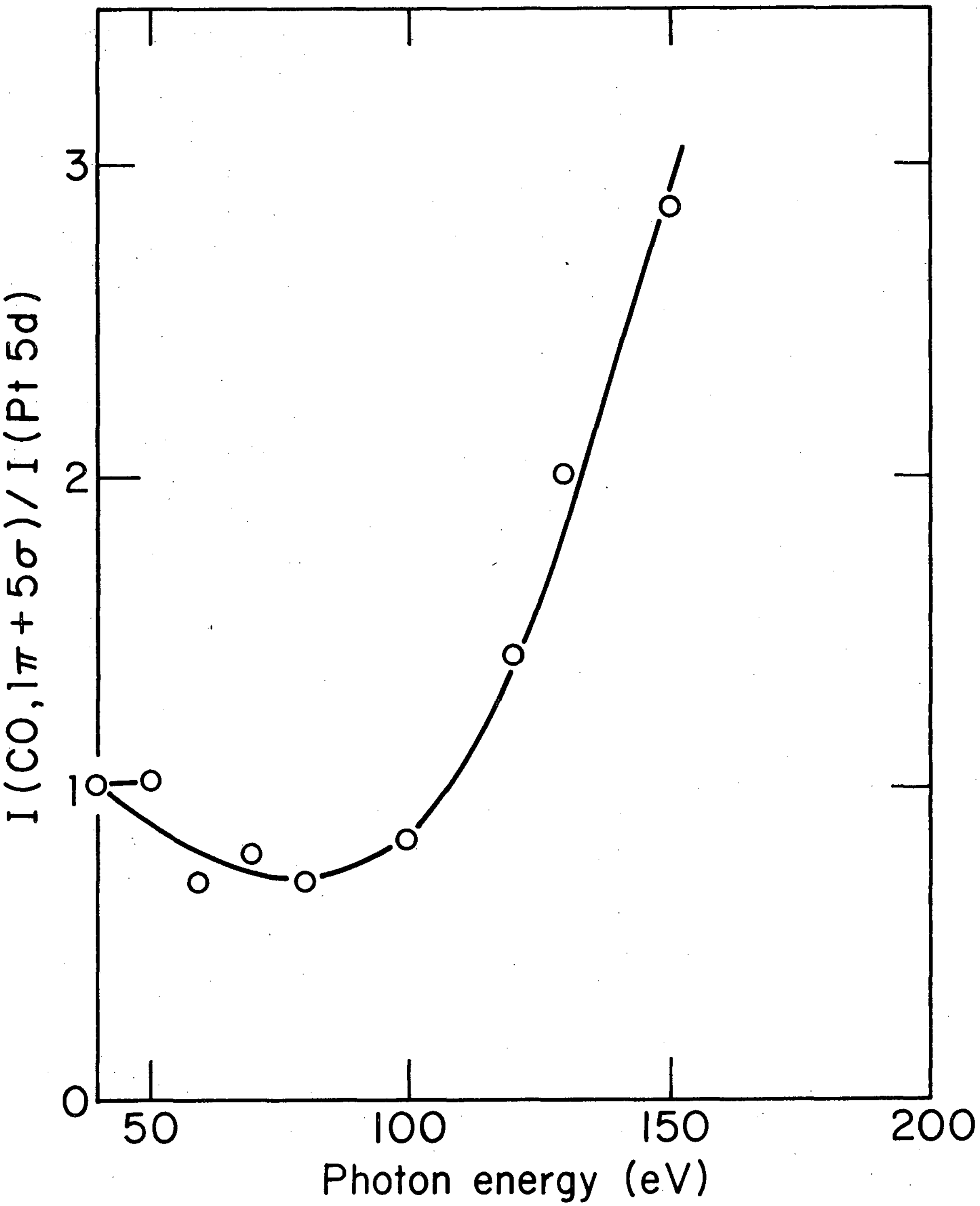

XBL 763-2484

Fig. 18

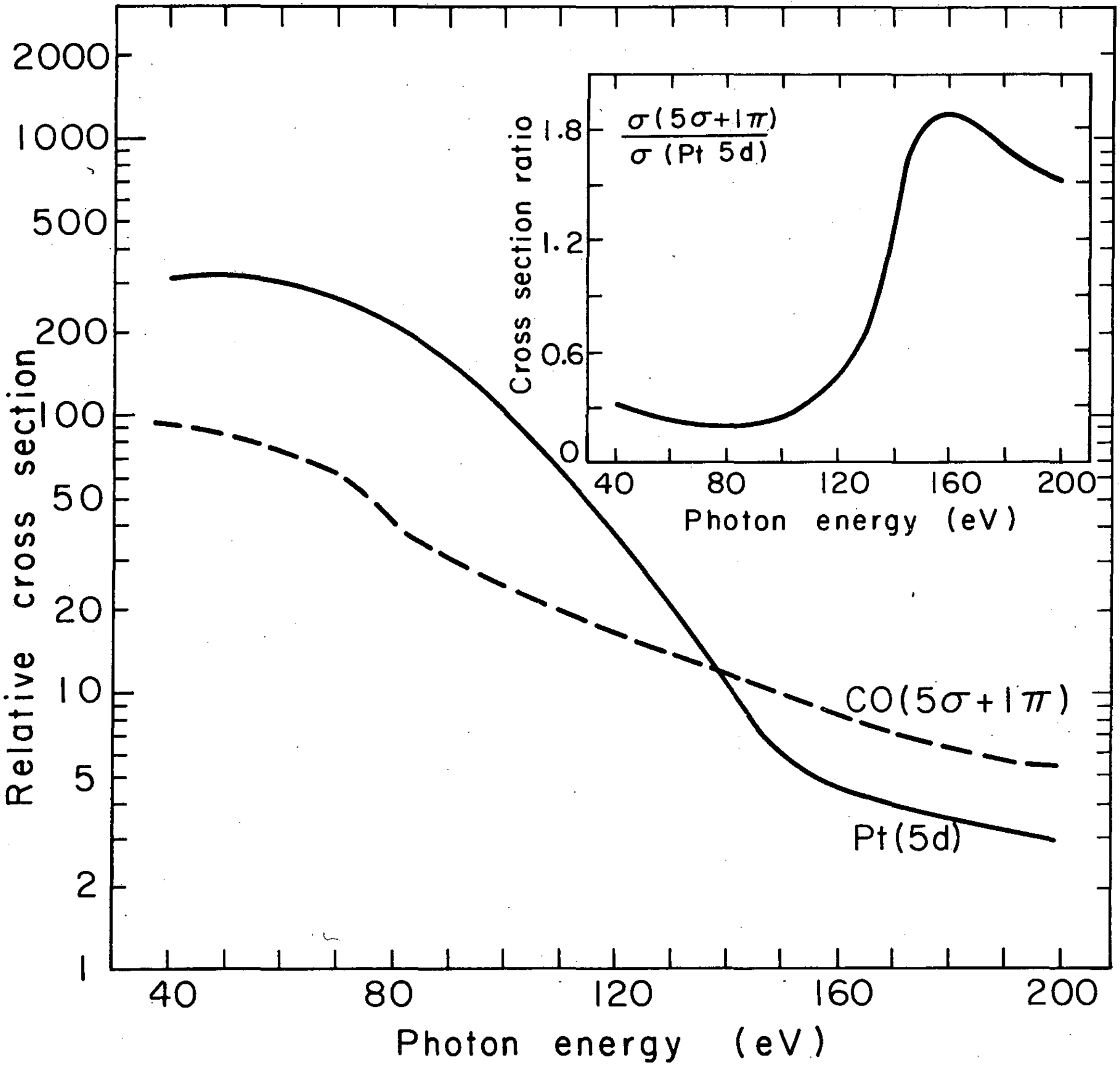

XBL 764-2786

Fig. 19

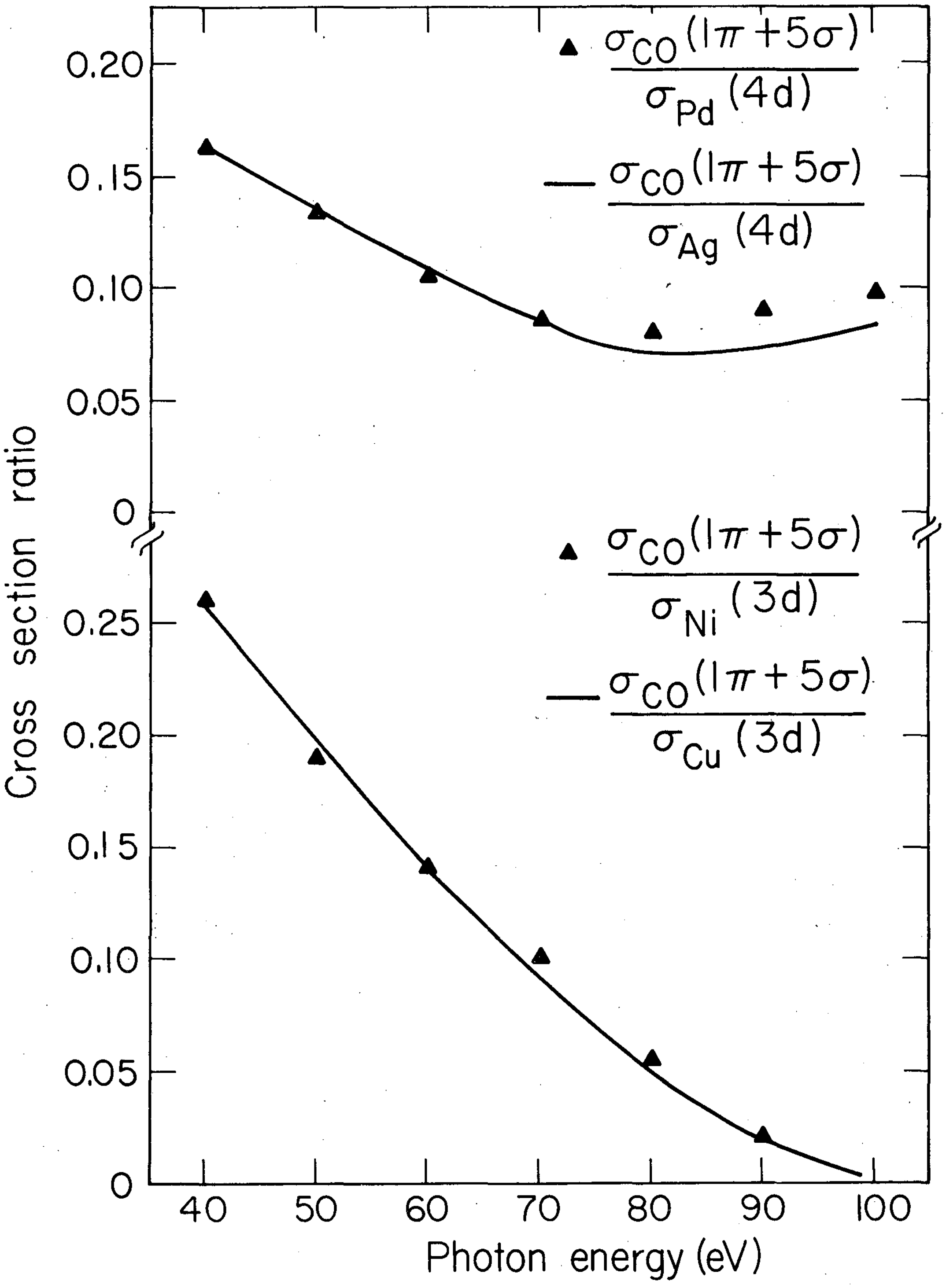

Fig. 20 XBL 775-1023

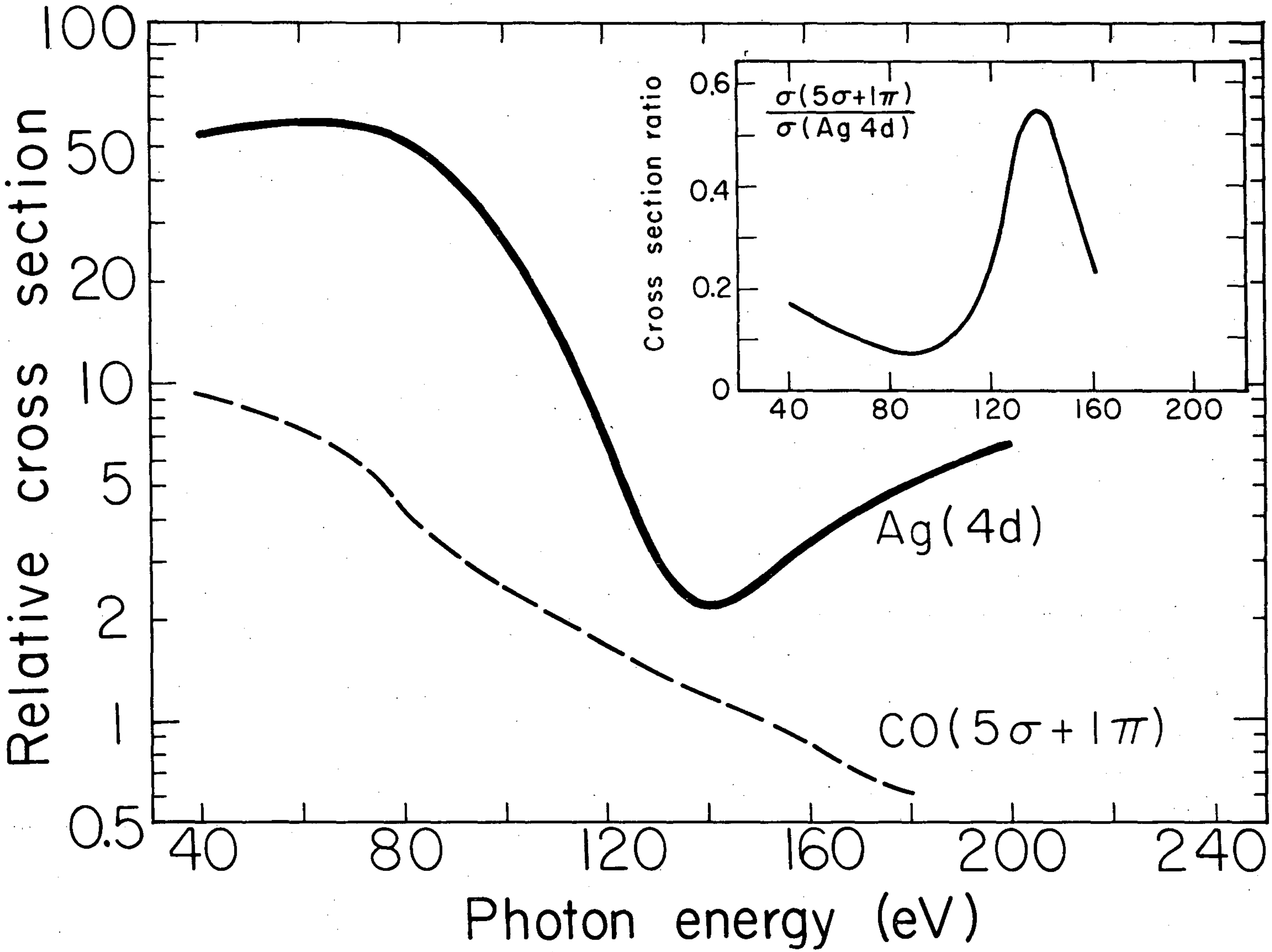

Fig. 21

XBL776-1114

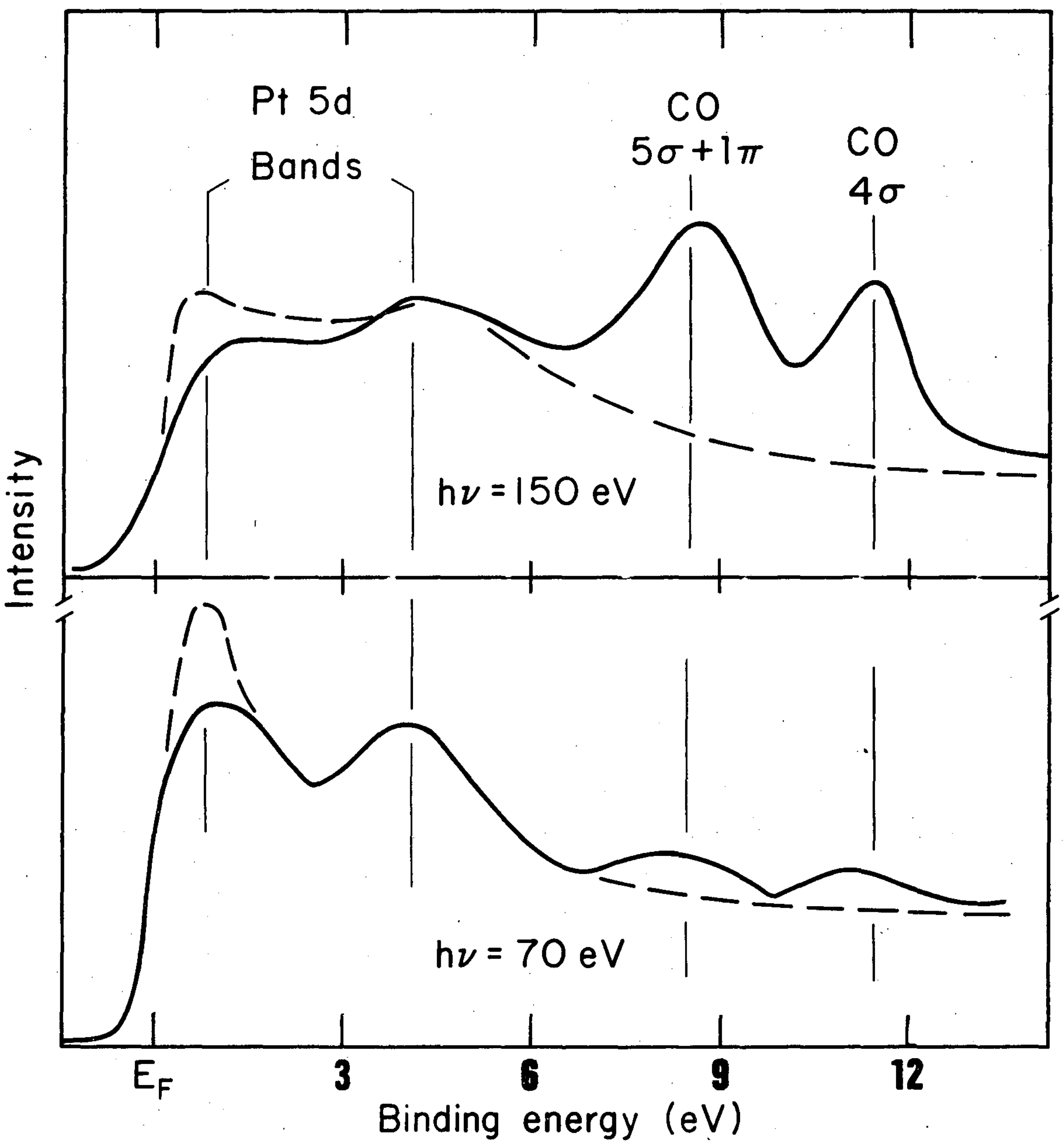

Fig. 22

XBL763-2485

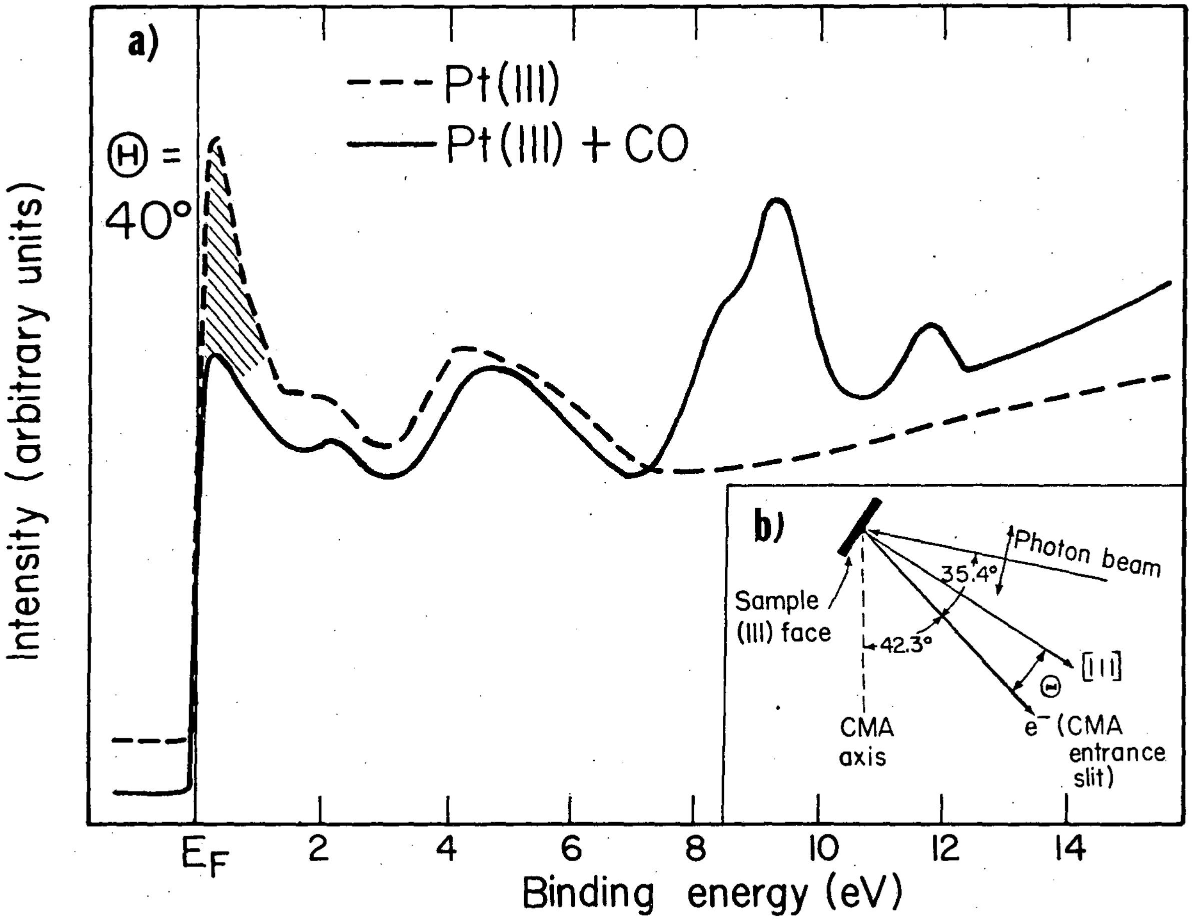

XBL 775-1021

Fig. 23

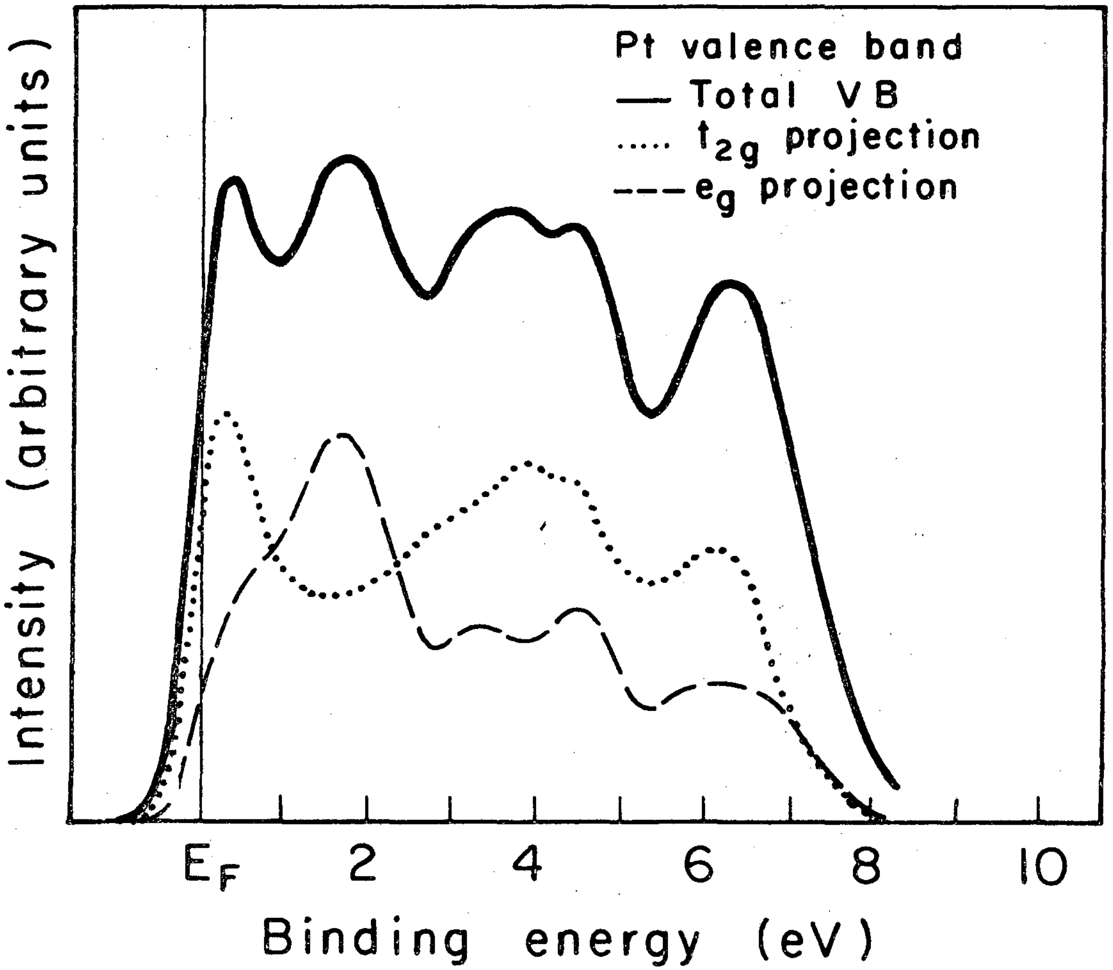

Fig. 24

XBL 764-2737

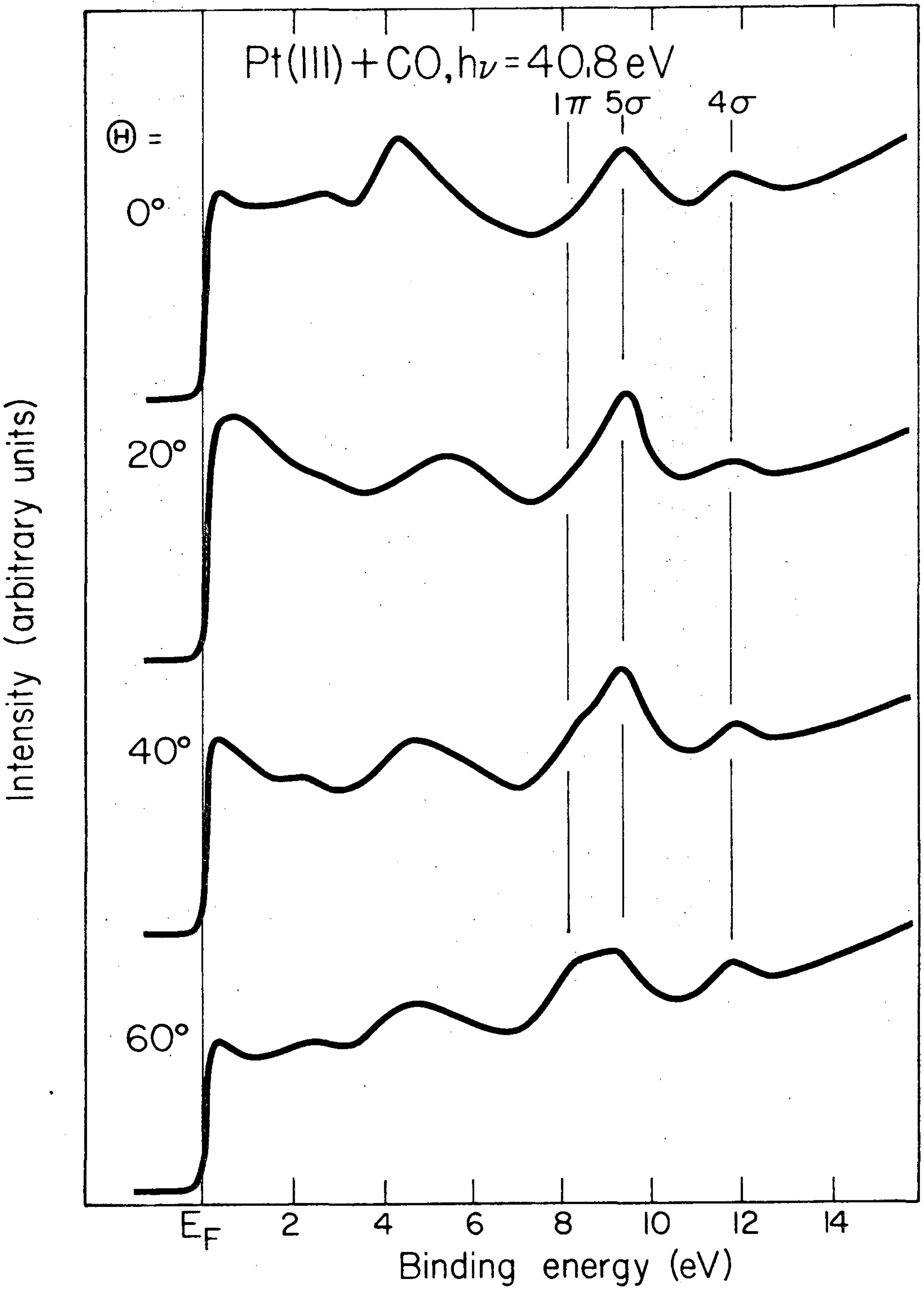

Fig. 25

XBL 775-1018

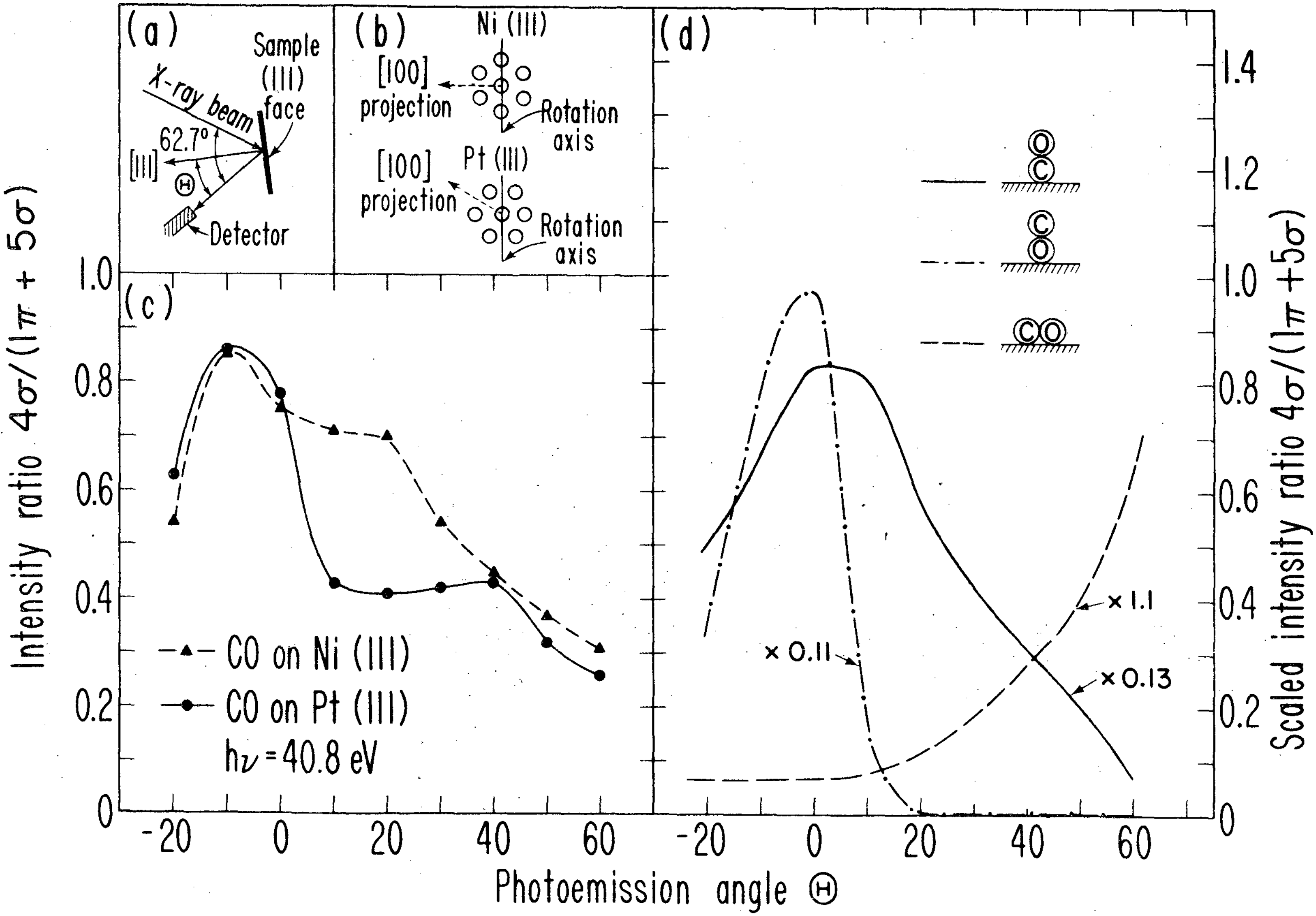

Fig. 26

XBL 769-3919

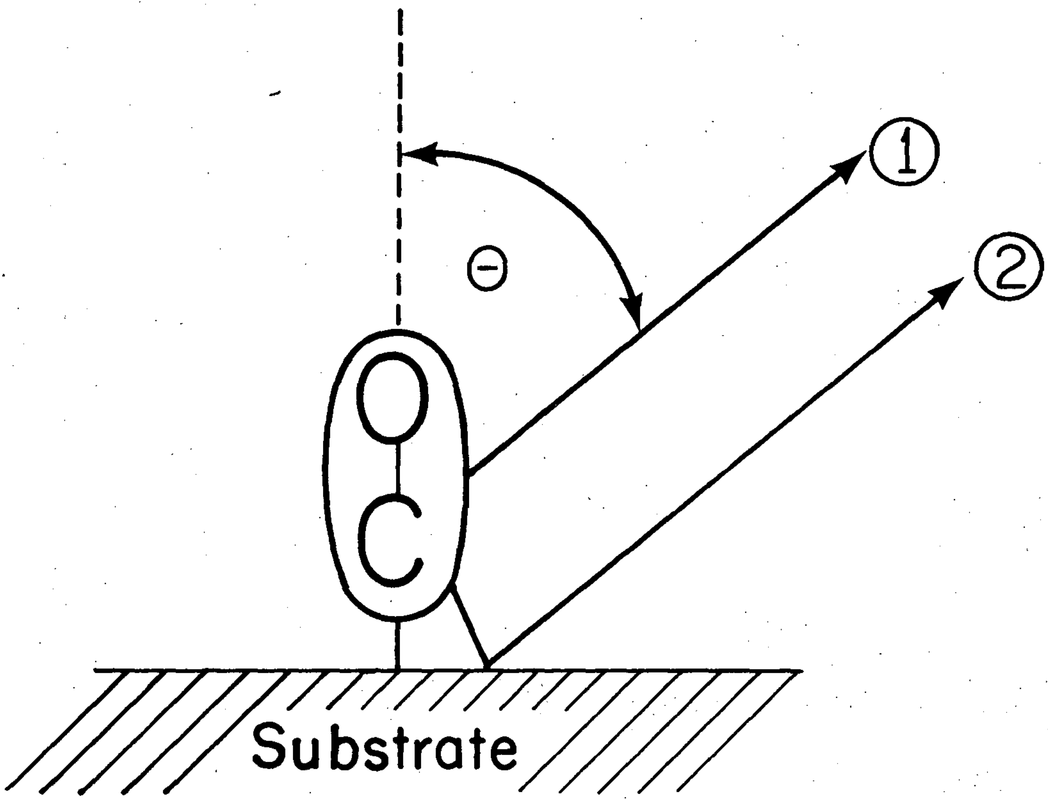

XBL 7611-4377

Fig. 27

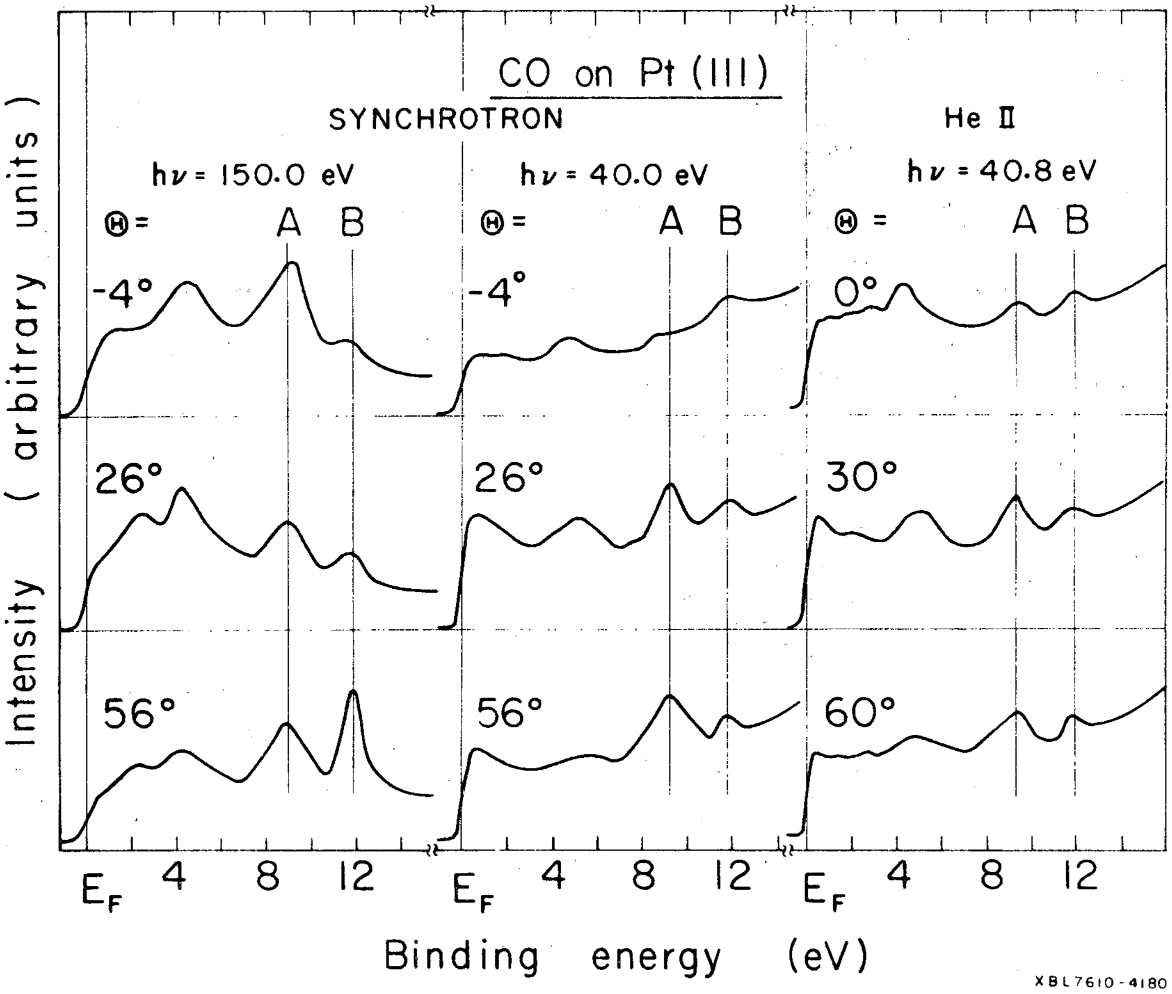
CO on Pt (III)
SYNCHROTRON
hν = 150.0 eV
hν = 40.0 eV
He II
hν = 40.8 eV
Θ =
A
B
-4°
26°
56°
-4°
26°
56°
0°
30°
60°
Intensity (arbitrary units)
E_F
4
8
12
Binding energy (eV)
XBL7610-4180

Fig. 28

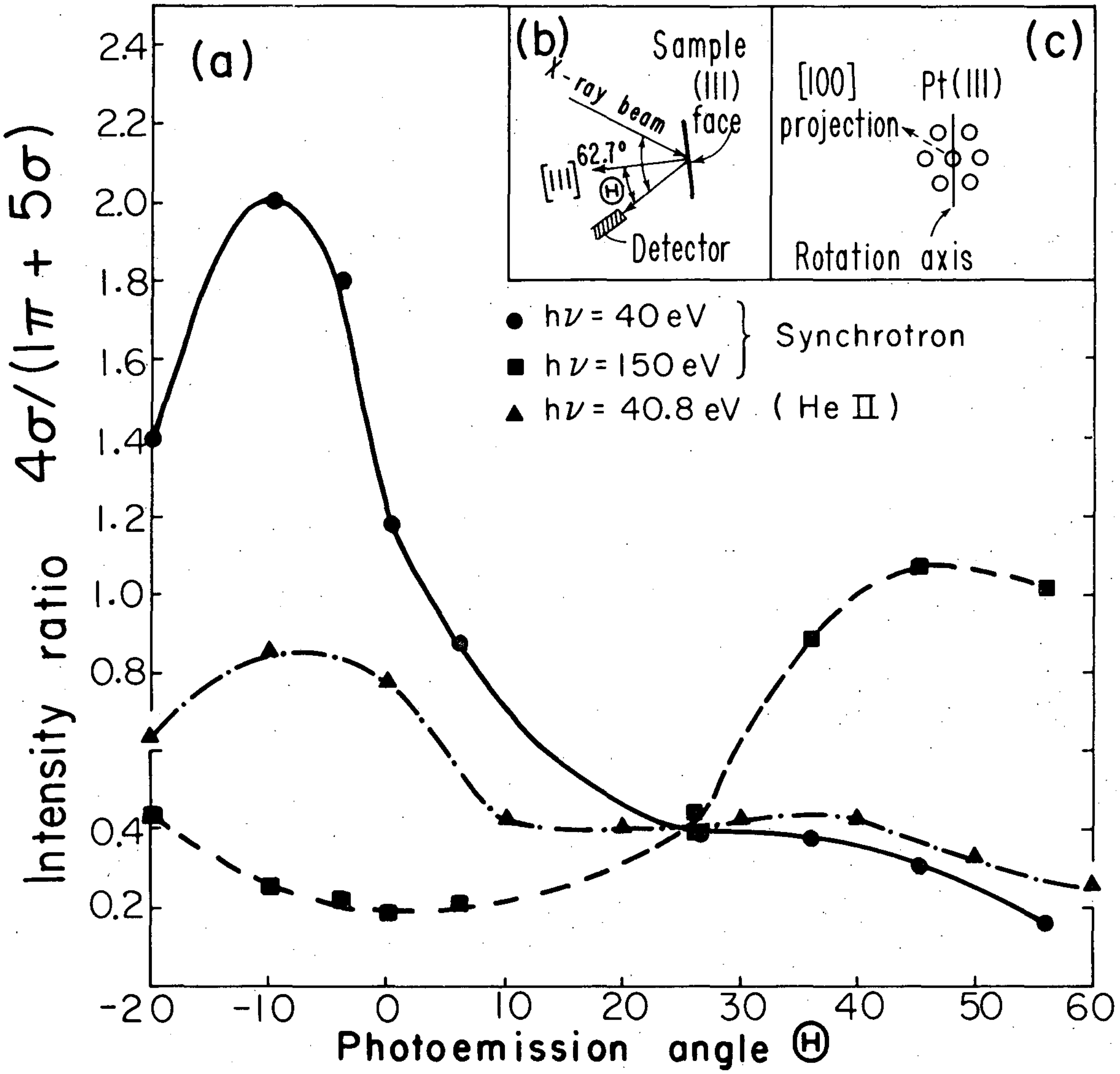

Fig. 29

XBL769-4026

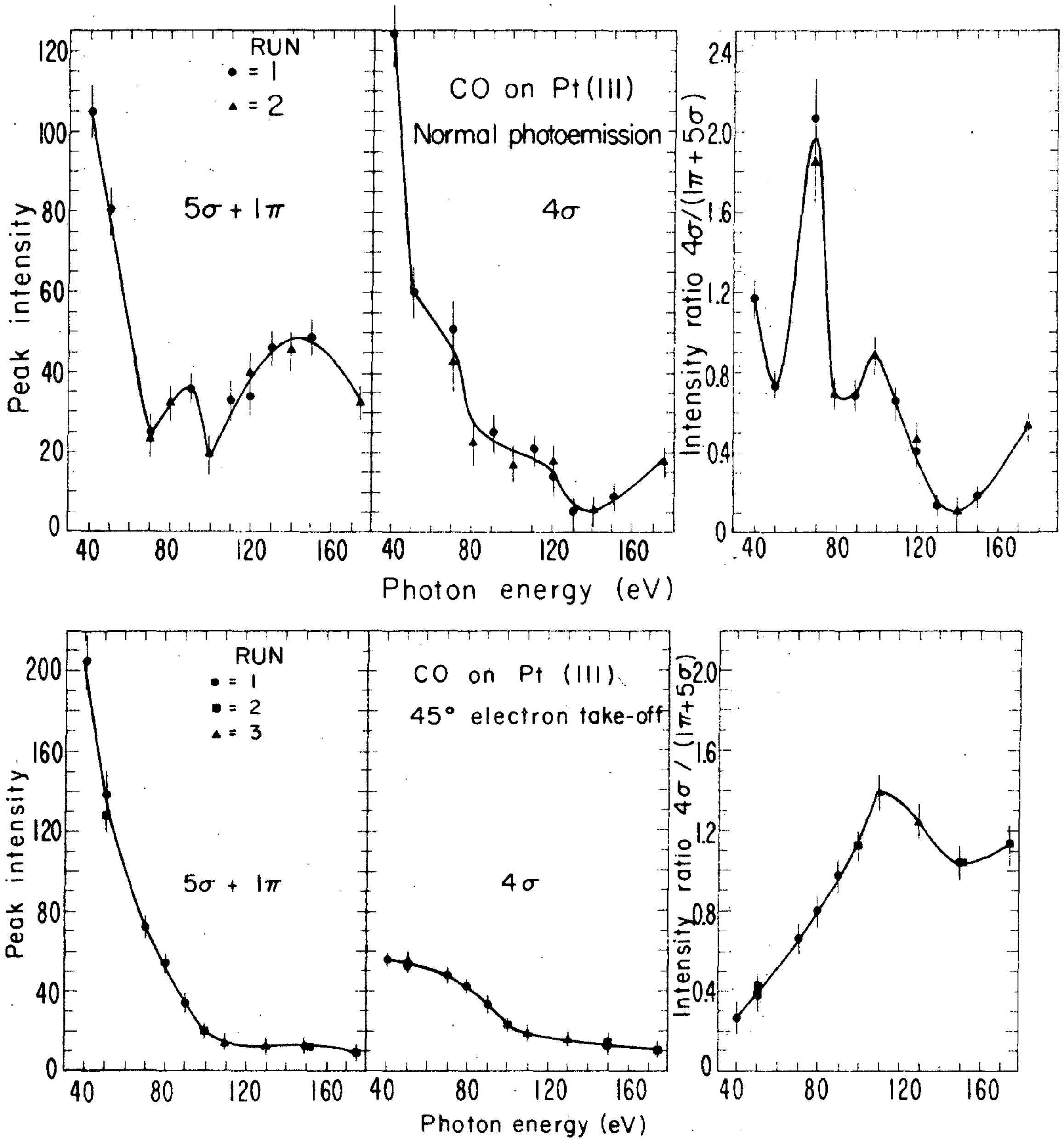

XBL 774-8535

Fig. 30

TECHNICAL INFORMATION DEPARTMENT
LAWRENCE BERKELEY LABORATORY
UNIVERSITY OF CALIFORNIA
BERKELEY, CALIFORNIA 94720